AGU ADVANCING EARTH AND SPACE SCIENCES

Tectonics®

RESEARCH ARTICLE
10.1029/2025TC009276

Spatial and Temporal Evolution of Graben Formation During Rift Linkage Using Quantitative Geomorphology: Insights From Central Afar

Reha Chandresh[1], Alexander C. Whittaker[2], Rebecca E. Bell[2], Giacomo Corti[3], Gianmaria Tortelli[1], Alessandro La Rosa[4], Carolina Pagli[4], Federico Sani[1], and Derek Keir[1,5]

[1]Department of Earth Sciences, University of Florence, Florence, Italy, [2]Department of Earth Science and Engineering, Imperial College London, London, UK, [3]Institute of Geosciences and Earth Resources, National Research Council (CNR), Florence, Italy, [4]Department of Earth Sciences, University of Pisa, Pisa, Italy, [5]School of Ocean and Earth Science, University of Southampton, Southampton, UK

Key Points:

- We use quantitative geomorphology to investigate normal fault (graben) evolution in a zone of active rift linkage in the Afar Depression
- We estimate fault initiation ages and throw rates to study deformation patterns and add quantitative constraints on fault evolution models
- We show that the Dobi Graben is the present-day locus of extension, and the strain has focussed towards the center of the linkage zone

Supporting Information:

Supporting Information may be found in the online version of this article.

Correspondence to:

R. Chandresh,
reha.chandresh@unifi.it

Citation:

Chandresh, R., Whittaker, A. C., Bell, R. E., Corti, G., Tortelli, G., La Rosa, A., et al. (2026). Spatial and temporal evolution of graben formation during rift linkage using quantitative geomorphology: Insights from Central Afar. *Tectonics*, *45*, e2025TC009276. https://doi.org/10.1029/2025TC009276

Received 10 NOV 2025
Accepted 6 APR 2026

Author Contributions:

Conceptualization: Reha Chandresh, Alexander C. Whittaker, Rebecca E. Bell, Giacomo Corti, Derek Keir
Data curation: Reha Chandresh
Formal analysis: Reha Chandresh
Funding acquisition: Alexander C. Whittaker, Rebecca E. Bell, Giacomo Corti, Federico Sani, Derek Keir
Investigation: Reha Chandresh
Methodology: Reha Chandresh, Alexander C. Whittaker, Rebecca E. Bell, Derek Keir
Project administration: Alexander C. Whittaker, Rebecca E. Bell, Giacomo Corti, Federico Sani, Derek Keir

Abstract Quantifying fault slip rates and resolving rift segment linkage mechanisms is important for understanding the evolution of magma-rich rift systems and the broader processes of continental break-up. In tectonically and volcanically active rifts, such as Afar, there is commonly a lack of quantitative, observational constraints on long-term fault system evolution and linkage. Quantitative geomorphology has proven effective in magma-poor rifts, yet its application in magma-rich contexts remains limited. In this study, we analyze 26 river catchments crossing active normal faults across seven major grabens in Central Afar. Using integrated geomorphic and topographic methods including stream power law analyses, knickpoint retreat metrics and swath profiles, we quantify landscape signals of tectonic activity and construct a spatial model of graben evolution. Our results show that rift linkage in Afar has been active for at least 3 Myr, with individual grabens accommodating extension over timescales of 0.5–1.0 Myr. Multiple grabens are commonly active synchronously, but integrating the graben initiation ages with their measured fault slip rate shows that most extension localizes through the center of the linkage zone. Notably, the Dobi Graben, in the center of the linkage zone, exhibits the youngest graben formation age and highest throw rates in the region of 0.4–0.8 mm/yr, implying it is the locus of present-day deformation. Our results provide the first quantitative constraints on spatio-temporal graben evolution in Central Afar, showing that extension due to rift linkage is primarily accommodated by en-echelon, normal fault-bound graben systems with the deformation progressively localizing through time.

Plain Language Summary Continental rifts are areas where the Earth's continents are being stretched and thinned by tectonic plates moving apart, leading to the formation of a rift valley and eventually a new ocean. In the Afar Depression in the Horn of Africa, three major rifts link, making it an area of active earthquake activity, leading to the formation of normal faults and grabens (cracks in the Earth's surface). While scientists accept this theory, not much work has been done in using real-world measurements to properly constrain how long these processes take. In this study, we use river systems to understand how the landscapes in the region respond to tectonic activity—that is, how river profiles have changed through time due to the movement and uplift on the faults. Knickpoints, breaks in channel slopes, are good records of faulting, and their formation age tells us about the age of fault initiation. We show that the faulting progresses towards the center of the depression. One of the central grabens—Dobi—is the most active, with fault throw (movement) rates of 0.4–0.8 mm/yr. Therefore, this is currently the most active with the largest concentration of earthquake activity.

1. Introduction

Continental rifts are zones of lithospheric extension, where deformation occurs through a complex, multi-stage process of the initiation, evolution, and linkage of the rift segments, potentially culminating in continental break-up (Brune et al., 2023; Neuharth et al., 2022). Depending on their geologic and geodynamic setting, rift systems display a spectrum of various structural styles and controls, ranging from fault-dominated (magma-poor) to magma-dominated systems showing an interplay between fault activity and magmatism (Dan et al., 2025; Merle, 2011). In most continental rift systems, extension and deformation are accommodated by the development of a complex array of normal faults and the initiation, propagation, and linkage of these fault segments controls

Supervision: Alexander C. Whittaker, Rebecca E. Bell, Giacomo Corti, Derek Keir
Validation: Gianmaria Tortelli, Alessandro La Rosa, Carolina Pagli
Visualization: Reha Chandresh
Writing – original draft: Reha Chandresh
Writing – review & editing: Reha Chandresh, Alexander C. Whittaker, Rebecca E. Bell, Giacomo Corti, Gianmaria Tortelli, Alessandro La Rosa, Carolina Pagli, Federico Sani, Derek Keir

basin morphology, sediment distribution, seismic hazard and the localization of subsurface resources such as geothermal energy, hydrocarbons and natural hydrogen (Cherkose et al., 2023; Dambly et al., 2023; Jolie et al., 2021; Ledésert et al., 2021; Olivia et al., 2019; Pan et al., 2022; Zwaan et al., 2024). Consequently, an understanding of such fault systems not only provides critical insights into the temporal and spatial evolution of rifting processes but also helps to address challenges related to energy security and natural hazard resilience.

A major challenge in magma-rich rifts is to understand the growth and evolution of fault networks over space and time. This can be attributed to the fact that in magma-rich rift settings, extension is accommodated not only by faulting but also by intrusive processes such as diking (Bialas et al., 2010; Ebinger & Casey, 2001; Hurman et al., 2023), which can make it challenging to distinguish tectonic deformation from magmatic contributions (e.g., Siegburg et al., 2020). Frequent, volcanic activity can complicate bedrock strength analysis and knickpoint retreat metrics, obscure fault traces, and modify landscapes. Despite these challenges, faulting remains a critical mechanism for accommodating extension throughout the lifecycle of magma-rich rifts (Bastow & Keir, 2011; Corti, 2009; Ebinger & Casey, 2001; Hurman et al., 2023; Muirhead et al., 2016; Rowland et al., 2007), therefore, making the study of active normal fault growth and interaction patterns crucial in our understanding of the evolution of continental rift processes. Particularly, in the Afar Depression, Ethiopia, the mechanisms governing rift linkage are not well understood due to the lack of structural-based measurements and shallow sub-surface data such as seismic reflection profiles. The Red Sea (RS), Gulf of Aden (GoA) and East African Rift (EAR) systems link in the Afar Depression, and multiple normal fault-bound graben systems in the center of the depression accommodate the extension and deformation in the linkage zone (Acocella et al., 2008). Most past work in the region has focussed on understanding the role of magmatism in the rifting processes (Barberi & Varet, 1977; Chernet et al., 1998; Kendall et al., 2005; Tortelli et al., 2022, 2025a, 2025b; Watts et al., 2025) but there is limited work on the role of the graben systems in the accommodation of extension. While numerical models based on geodesy, strain rate analysis and paleomagnetism have provided valuable conceptual insights into rift development and linkage timescales (La Rosa et al., 2025; Manighetti et al., 1998, 2001; Muluneh et al., 2024; Pagli et al., 2019; Tapponnier et al., 1990), direct structural constraints on fault initiation ages are lacking, and the chronology of graben development remains unresolved.

Quantitative geomorphology has emerged as a powerful approach for investigating landscape dynamics in regions of active normal faulting. Analyses of river longitudinal profiles, hydraulic geometry, drainage divide migration, and the spatial distribution of tectonic knickpoints have increasingly been used to trace fault growth and interaction over time (Attal et al., 2008; Boulton & Whittaker, 2009; Gallen & Wegmann, 2017; Gasparini et al., 2016; Kirby & Whipple, 2001, 2012; Roda-Boluda & Whittaker, 2018; Stüwe et al., 2022; Whipple & Tucker, 2002; Whittaker et al., 2007a, Whittaker et al., 2007b). These metrics, typically contextualized with respect to the stream power law, can provide insights into how fluvial systems respond to active tectonics, record long-term uplift, and constrain the timing of landscape adjustment (Allen et al., 2013; Boulton et al., 2014; Kent et al., 2021; Miller et al., 2012; Snyder et al., 2000, 2003; Whittaker et al., 2007a, Whittaker et al., 2007b; Zondervan et al., 2020). Furthermore, relationships between knickpoint height, formation age, and fault relief have been used to quantify fault growth and linkage patterns, reinforcing the utility of transient landscape analysis in constraining fault evolution timescales, particularly where bedrock erodibility can be estimated or constrained. Knickpoints act as geomorphic markers of tectonic perturbation, often forming in response to fault initiation, evolution and linkage, differential uplift, or changes in the slip rate (Whittaker, 2012). The spatial distribution of the knickpoints and the rates at which they migrate upstream of a channel have been used to understand the propagation of normal faults through time, and the patterns of deformation associated with activity on these faults (Roda-Boluda & Whittaker, 2017; Whittaker, 2012; Whittaker & Walker, 2015), as well as the scaling relationship between knickpoint retreat rates and fault throw (Whittaker & Boulton, 2012). For example, Pavano et al. (2016) have used catchment slope-area analysis and knickpoint ages to constrain non-uniform fault uplift patterns in northeastern Sicily, and slope-break knickpoints have been used to infer fault slip rates and segment linkage timescales in the Gediz Graben in Turkey (Kent et al., 2017, 2021). A coupled approach between structural and geomorphic analysis focusing on knickzones, notches, the magnitude of incision, bedrock properties, stream network mapping and fault profiles has been used to understand the reconstruct the growth and evolution of normal fault arrays in the Canyonlands Graben, Needles District, Utah (Commins et al., 2005; Gieger, 2014; Trudgill, 2002). Similarly, Sembroni et al. (2016) have used topography data, river long profiles and knickpoint celerity models to investigate the relationship between mantle dynamics and surface processes in the Ethiopian Highlands, NW Ethiopia, and successfully provided a framework of landscape evolution in the region.

While these previous studies have successfully applied quantitative geomorphology techniques to investigate fault growth and landscape response in fault-dominated (magma-poor) rifts, such approaches remain significantly under-explored in magma-rich rifts. Recent studies have demonstrated that it is possible to extract insights into normal fault evolution from topography in volcanically active rift settings such as the East African rift (e.g., Wedmore et al., 2024; Williams et al., 2022), although little work to date incorporates the full suite of geomorphology tools that could add additional quantitative constraints on fault activity and landscape response over time and space.

Central Afar is a complex zone of magma-rich rifting and is widely recognized as a key natural laboratory to study present-day rift linkage and continental break-up (Bastow & Keir, 2011; Chauvet et al., 2023; Keir et al., 2013; Rime et al., 2024; Wolfenden et al., 2005), yet a gap exists in the research around two key aspects: (a) the evolution patterns of normal fault-bound graben systems within the rift linkage zone; and (b) the potential of quantitative geomorphology techniques to quantify fault growth and evolution timescales in magma-rich continental rift systems. This study therefore aims to address the gap by integrating geomorphic and structural analyses to constrain the initiation and spatio-temporal evolution of the graben systems in Central Afar where the timing of fault initiation is poorly constrained.

In particular, we: (a) quantify landscape signals of normal fault activity over million-year timescales using a combination of swath and long profile analysis; (b) constrain the timing of graben initiation and rate of fault growth—using a stream power model to estimate bedrock erodibility and knickpoint formation timescales coupled with maximum age constraints on fault initiation from surface lava flow ages and erosion rate data; and (c) Integrate knickpoint retreat metrics with fault geometry and relief, to constrain the spatio-temporal dynamics of fault growth and rift linkage. Knickpoints preserved in the geomorphic record serve as proxies for fault-driven base level changes, allowing us to extract temporal information on fault growth and segment linkage. In so doing, we provide new constraints on the timing and evolution in seven grabens associated with the rift linkage zone in the Afar Depression.

2. Geological Setting of the Afar Depression

The Afar Depression, located in the Horn of Africa (Figure 1a), spans an area of ∼150,000 square kilometers across northeast Ethiopia, southern Eritrea, and western Djibouti. It is bound by the Ethiopian plateau to the west, Somalian plateau to the south and the Danakil block to the North (Figure 1b). The Afar Depression is a classic triple junction of the Arabian, Nubian (African), and Somalian plates (Figure 1a). Three active divergent plate boundaries—the Red Sea rift (RS), the Gulf of Aden rift (GoA), and the East African Rift System (EARS)—meet in this region (Maestrelli et al., 2024). The northernmost segment of the EARS is the Main Ethiopian Rift (MER) (Figure 1a). The Afar Depression is also one of the few places in the world that has a plume upwelling associated with the continental rifting—the Afar Plume, that impinges on the base of the thinning plate. The anomalously warm mantle enhances the rift related magmatism and volcanic activity in the region (Bastow et al., 2005; Watts et al., 2025). This unique configuration makes the Afar Depression an excellent natural laboratory for studying continental rift processes and the evolution and linkage of continental rift systems.

Geodetic data show extension across the Red Sea rift at ∼18 mm/yr (Arabian–Nubian), ∼15 mm/yr across the Gulf of Aden rift (Arabian–Somalian), and ∼6 mm/yr across the Main Ethiopian Rift (Nubian–Somalian) (McClusky et al., 2010; Saria et al., 2014). Extension across the Red Sea and Gulf of Aden rifts is directed NE–SW, interacting with the E–W-trending northern Main Ethiopian Rift in southern Afar (Beyene & Abdelsalam, 2005).

Rift development in Afar was diachronous: Initial rifting began in the Oligocene (∼30 Ma), forming large border faults in the Gulf of Aden–Red Sea system and marking the onset of extension (Wolfenden et al., 2005). This phase coincided with the Ethiopian Flood Basalt event, linked to the Afar plume (∼31–29 Ma) (Leroy et al., 2010; McClusky et al., 2010; Wolfenden et al., 2005; Zwaan et al., 2020). Continued rifting through the Miocene led to the development of distinct continental rift segments and evolving fault architectures, and the accommodation of extensional strain through smaller-scale faults and dike intrusions (Wolfenden et al., 2005). Over the past ∼4 million years, rifting in Afar has become progressively localized to the magmatic segments (Barberi &

10.1029/2025TC009276

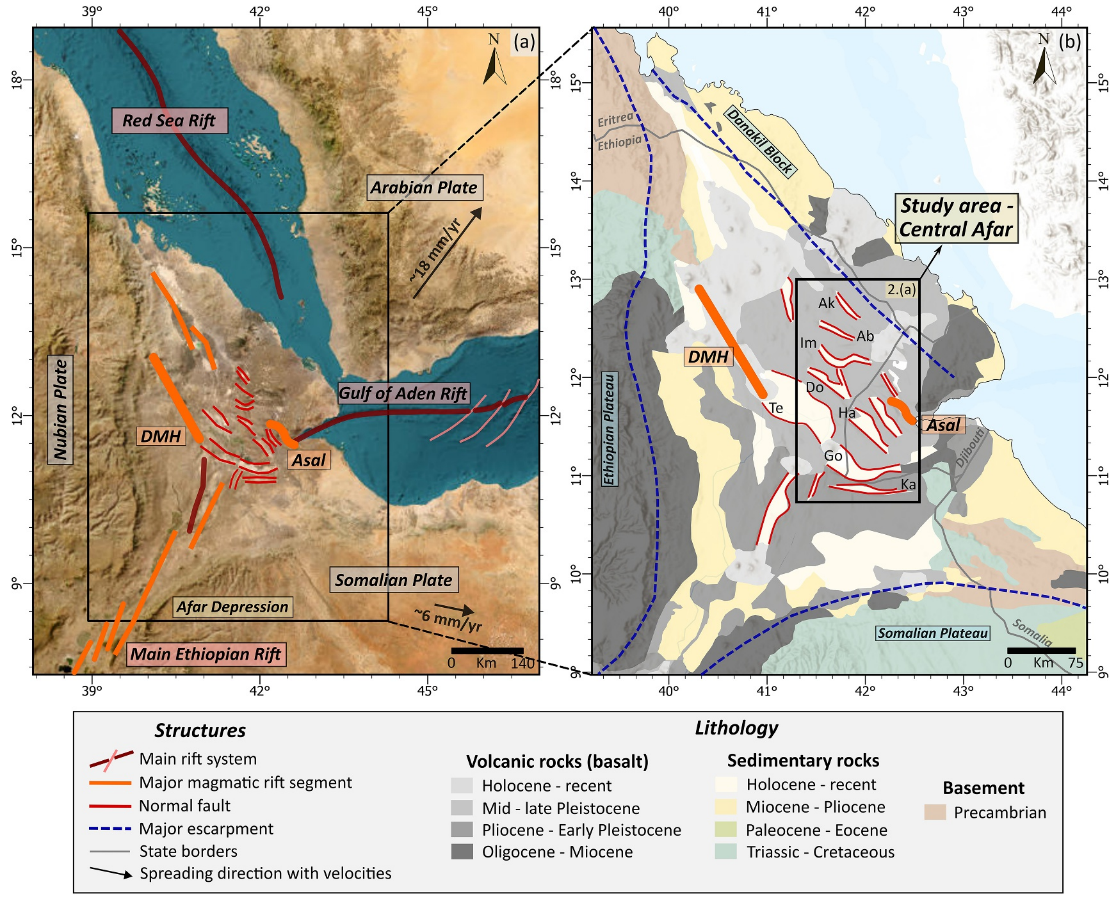

Figure 1. (a) Simplified topographic map of the Horn of Africa, showing the three major rift systems of the Afar Triple Junction, and their tectonic (red) and magmatic (orange) segments (derived from Manighetti et al., 1998; Beyene & Abdelsalam, 2005). Current plate spreading velocities derived from McClusky et al., 2010; Saria et al., 2014. (b) Simplified lithological map of the Afar Depression (lithology boundaries derived from Rime et al., 2023). The map shows extent of the Depression and the major tectonic segments that is, normal fault bound graben systems (red). Ak = Akulle Graben; Ab = Ab'a Graben; Im = Immino Graben; Do = Dobi Graben; Ha = Hanle Graben; Go = Goba'ad Graben; Ka = Kalkle Graben; Te = Tendaho Graben.

Varet, 1977; Doubre et al., 2007; Hayward & Ebinger, 1996; Manighetti et al., 1998; Rime et al., 2023; Tortelli et al., 2025a, Tortelli et al., 2025b), where extension is accommodated by dike intrusion and dike-induced faulting (Moore et al., 2021; Rowland et al., 2007). The period from the Pliocene to present, has seen extensive volcanic activity and the emplacement of volcanic units throughout the center of the depression (Corti et al., 2015; Tortelli et al., 2025a, Tortelli et al., 2025b; Wolfenden et al., 2005).

Central Afar is a complex zone of rift linkage between the Dabbahu-Manda-Harraro (DMH) magmatic segment of the Red Sea rift and the Asal magmatic segment of the Gulf of Aden rift (Figure 1). This zone of linkage between both magmatic segments is marked by a complex array of fault systems and active deformation (Muluneh et al., 2024). These include kilometer-scale grabens bound by high-angle normal faults, smaller cross-cutting grabens, and faults with varying orientations (Figure 1). The principal grabens (Figure 1b), typically span 30–60 km in length and 7–10 km in width, trend predominantly W-NW—E-SE and accommodate active crustal extension through faulting (Doubre et al., 2007; Pagli et al., 2014, 2019). Subordinate N-S grabens and minor faults crosscut the major grabens, resulting in a highly segmented fault architecture across the region (Figure 1b).

Although active linkage between these two magmatic rift segments has been ongoing since the last ~3–5 My (Beyene & Abdelsalam, 2005; Manighetti et al., 1998), the chronology of graben formation and mechanism of linkage remains debated. Older models based on paleomagnetic analyses (Kidane et al., 2003; Manighetti et al., 1998, 2001; Muluneh et al., 2013; Tapponnier et al., 1990) have proposed that the rift linkage occurred through overlap between the southward propagating DMH (RS) segment and northward propagating Asal (GoA) segment. The shear was accommodated by clockwise block rotation with slip occurring along rift parallel sinistral

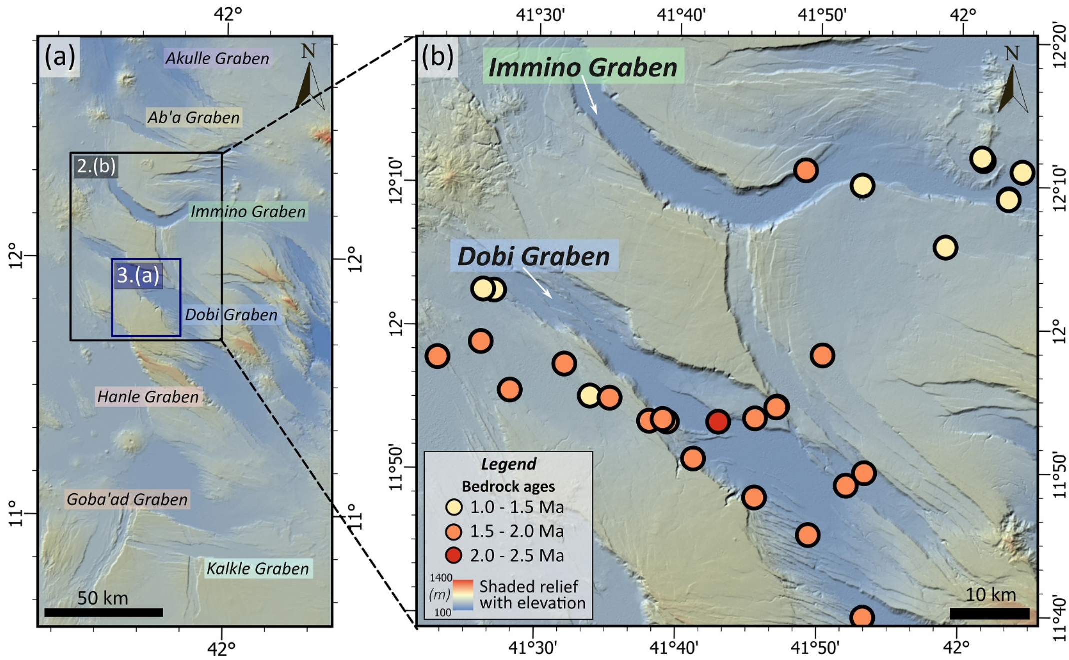

Figure 2. (a) Map of the study area, corresponding to the inset marker in Figure 1b. The blue inset marker corresponds to Figure 3a. (b) Spatial distribution of published ages for the Afar Stratoid Series (Lahitte et al., 2003; Tortelli et al., 2025a, Tortelli et al., 2025b). All data are displayed over a shaded relief and elevation map derived from the 30m DEM in ArcGIS Pro.

strike slip faults, that is, bookshelf faulting (Courtillot et al., 1984; Tapponnier et al., 1990). However, recent numerical modeling studies (Duclaux et al., 2020; Muluneh et al., 2024), have shown that during the initial 2–3 My, linkage was accommodated by overlapping rift propagation, enabling the clockwise rotation of the linked block without bookshelf faulting. Over time, this evolved into direct linkage and progressive localization of extension along left-stepping en-echelon basins, and the zone of direct linkage is shown to be bound to the N and S by rift-perpendicular shear zones and strike-slip faults. These results are consistent with the current strain distribution modeled from InSAR and GNSS (Doubre et al., 2017; La Rosa et al., 2025; Muluneh et al., 2024; Pagli et al., 2019).

The tectonic evolution of the Afar Depression is closely tied to its lithological framework. Extensive geochemical and isotopic analyses (Barberi et al., 1972; Chernet et al., 1998; Lahitte et al., 2003; Teklay et al., 2010; Tortelli et al., 2022, 2025a, 2025b) and geological mapping (Rime et al., 2022) reveal that Central and Southern Afar are predominantly composed of the Afar Stratoid Series. These mainly basaltic flows were emplaced during the Pliocene to early Pleistocene in Southern Afar, representing the Lower Stratoid Series. In Central and Northern Afar, the primary focus of this study (Figure 1b), the Upper Stratoid Series dominates and is characterized by a voluminous, predominantly basaltic succession emplaced over a well-defined period from the mid-to-late Pleistocene (White et al., 2006). This formed a regionally extensive bedrock plateau which was subsequently dissected and offset by extensive faulting throughout the Afar Depression (Acocella et al., 2008, 2010). Stratigraphic characterizations (Barberi et al., 1972; Barberi & Varet, 1977; Kidane et al., 2003; Rime et al., 2022), indicate that the Stratoid flows are laterally continuous at a regional scale of several hundred kilometers. Although minor compositional and petrological variations occur locally, the Upper Stratoid series is considered to be largely chemically homogeneous (Acocella, 2010; Tortelli et al., 2022, 2024).

The emplacement of the Stratoid Series is associated with diachronous magmatic activity linked to rift migration and localization (Nelson et al., 2012; Tortelli et al., 2025a, Tortelli et al., 2025b). K/Ar isotopic geochronology studies from parts of Central Afar have shown that the ages of the different flows range from approximately 1.0–2.5 Ma (Figure 2b) (Feyissa et al., 2019; Lahitte et al., 2003; Tortelli et al., 2025a, Tortelli et al., 2025b), reflecting broadly uniform bedrock ages in this region.

The Afar region today is characterized by an extremely hot and arid climate, receiving less than 300 mm of annual rainfall. During the Pliocene—Early Pleistocene, intermittent increases in precipitation and humidity supported lake formation and the accumulation of lacustrine sediments (Abbate et al., 1995; Bonnefille et al., 2004; DiMaggio et al., 2015). Mid-late Pleistocene marked a shift towards more extreme aridity (Rime et al., 2023; Smail et al., 2025; Tierney et al., 2017; Trauth et al., 2005), and from the Holocene to the present, Afar's climate has remained persistently dry, largely due to its position in the rain shadow of the Ethiopian and Somalian highlands (Gasse et al., 1980; Gasse & Street, 1978).

Despite extensive research on rift kinematics role of magmatic segments and dyke intrusions in accommodating extension (Belachew et al., 2011; Keir et al., 2009), relatively little work has been conducted in Central Afar to quantify the spatio-temporal evolution of graben systems and their linkage patterns. Particularly, there is a lack of structural, quantitative constraints on the timing of fault initiation and growth across the region. Recently, Polun et al. (2024) made a first step towards addressing this gap by applying a landscape evolution model calibrated with terrestrial cosmogenic nuclide analyses to estimate fault initiation timescales within the Dobi graben; however, their study was limited to two river systems only, and a systematic analysis of multiple catchments in a regional context crossing faults remains outstanding. Therefore, this study aims to provide a more comprehensive analysis of fault initiation and evolution across multiple graben systems in Central Afar.

3. Methods

To study the landscape response to the continental rift associated normal fault growth and evolution, our study employs a combination of geomorphic and structural analysis of seven major graben systems in the Afar Depression, from North to South, the Akulle, Ab'a, Immino, Dobi, Hanle, Goba'ad, and Kalkle Grabens (Figure 1b, graben names as labeled in Pagli et al., 2019; Rime et al., 2023).

3.1. Catchment Analysis

The selection of river systems and catchments for this study was guided by a combination of geomorphological, structural, and hydrological criteria, aimed at isolating catchments that would reflect active tectonic processes, and therefore be suitable for quantitative geomorphology-based analysis. This was done using the 30m spatial resolution digital elevation models (Farr et al., 2007; NASA SRTM, 2013) from the Shuttle Radar Topography Mission (SRTM) data set, which were first processed in ArcGIS Pro using the spatial analyst and hydrology toolboxes to extract potential stream networks. This was followed by manual geomorphic mapping using high-resolution aerial imagery in Google Earth Pro to accurately identify flow networks and catchment boundaries. Catchments were selected where stream flow clearly originated on the top of the footwall of the graben bounding faults, and terminated within the graben, on the hangingwall. Another key criterion was the presence of a drainage network, including identifiable channel trunks and/or tributaries. Additional morphological identifiers of stream flow included the presence of incised canyons indicating sustained erosion, and the presence of fan-like deposits on the graben floor at the base of the incised canyons, interpreted as products of flow.

Based on these criteria, 26 river systems and their catchments were delineated across the seven graben systems within the study area (Figures 2 and 3). The DEMs of each catchment were subsequently fed into MATLAB, and further topographic and geomorphic analyses were done using the TopoToolbox functions (Schwanghart & Scherler, 2014).

For each catchment, a threshold value of 300 pixels was used to extract and create the stream network, giving a stream-forming drainage area threshold of 0.27 km^2. These thresholds were chosen to clearly pick out detailed stream features, including smaller tributaries, ensuring that there were no gaps in the main flow network and the analysis of geomorphic metrics could be conducted for all catchments. This threshold also corresponds well with the scale at which small headwater channels are visible in aerial imagery mapping on Google Earth Pro in the Afar region (>0.15 km^2). Using the PPS (Point Pattern on Stream networks) function in the TopoToolbox directory (Schwanghart et al., 2021), 100 spatially uniform sample points were identified along the main channel/trunk of each river system, and the elevation (in meters), upstream flow distance (in meters) and upstream drainage area (in square kilometers) was obtained for each point. Only fluvial catchments with drainage areas >3 km^2 were included in this study.

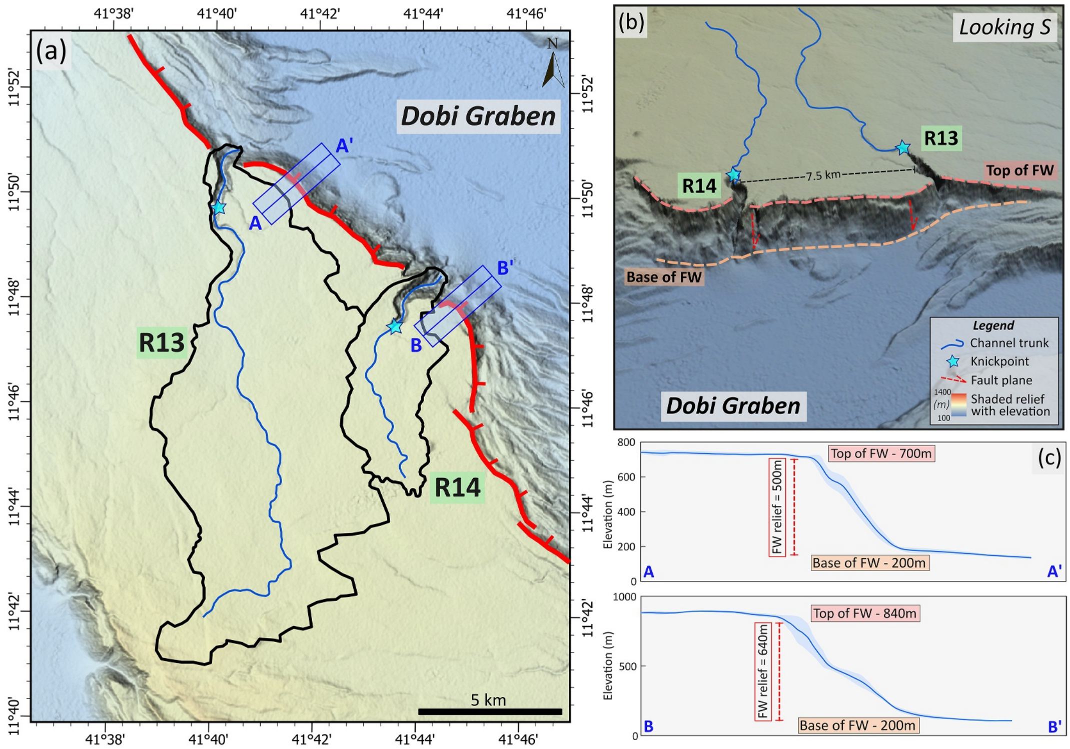

Figure 3. (a) Zoomed in view of catchments R13 and R14, from the Dobi Graben, used in the catchment analysis calculations as highlighted in Section 3.1. In Panel (a) corresponds to the blue inset marker in Figure 2a. The blue rectangles are the traces of the fault relief profiles in (c). (b) 3D view of the main graben bounding fault scarp and the canyons incised by R13 and R14. The blue stars show the location of the knickpoints. (c) Fault relief profiles to quantify the footwall height proximal to R13 and R14.

Using the TopoToolbox knickpoint finder function, the major knickpoints in each catchment were located, and added to the long profiles. The function identifies the knickpoints as sharp convex sections separating the otherwise concave (equilibrium) sections in the river long profiles (Schwanghart & Scherler, 2017). To assess sensitivity to DEM noise, we tested this function with specified tolerances of 10, 30, 50 and 100m, which span and exceed the vertical absolute error range of the SRTM 30m DEM (10–20m; Farr et al., 2007). The same major knickpoint was consistently identified along the channel trunk for all threshold values, and this feature was used as the slope-break knickpoint in our analyses. In addition, the knickpoints were located at zones that showed abrupt breaks in channel gradient (Whittaker & Walker, 2015). This was further validated by aerial imagery on Google Earth, and DEM mapping in ArcGIS Pro, following the knickpoint characterization work done by Zhou et al. (2024), in the Gulf of Corinth, Greece.

To facilitate visual and consistent comparison of rivers of different lengths and drainage areas, and to be able to visualize and compare knickpoint heights in each graben consistently, the river long profiles were normalized and scaled using:

$$d_{\text{norm}} = \frac{d}{L} \tag{1}$$

Where d_{norm} is the normalized distance downstream, d is the distance downstream from the point to the outlet, in meters and L is the total flow distance along the channel trunk. The outlet was chosen as the point where the river crosses the normal fault plane, and in cases where there were fan-like deposits are present at the base of the fault plane, the outlet was chosen to be at the top of the fan deposits (Figure 3).

Similarly, for the elevation:

$$z_{\text{norm}} = \frac{z - z_{\text{outlet}}}{z_{\max} - z_{\text{outlet}}} \tag{2}$$

Where z_{norm} is the normalized elevation, z is the elevation at the point in meters, z_{outlet} is the elevation of the river outlet in meters, and z_{max} is the maximum elevation point at the channel head, in meters.

3.2. Bedrock Erodibility and Knickpoint Propagation Analysis

To effectively constrain the knickpoint propagation timescales and compare knickpoint formation ages across the seven grabens, we treat the underlying bedrock as compositionally and mechanically uniform. Regional geological stratigraphic mapping shows that the bedrock in the study area is primarily composed of the Upper Stratoid Series (Barberi & Santacroce, 1980; Kidane et al., 2003; Rime et al., 2022, 2023), which are mainly basalts, laterally continuous, and emplaced across the region during the mid-late Pleistocene (Wolfenden et al., 2005). Although variations in flow sequences can occur locally, petrological, and geochemical studies demonstrate that the bedrock is largely homogeneous throughout the study area (Barberi & Varet, 1977; Feyissa et al., 2019; Tortelli et al., 2022, 2024). Published K-Ar geochronology-based ages for the Stratoid in Central Afar range from approximately 1.5–2.0 Ma proximal to the Dobi Graben (Figure 2b), and capture the variability associated with different flows and stratigraphic units, suggesting the absence of major lithological variability across all grabens. The absence of other spatially continuous age constraints and lithology or erodibility data sets across all grabens allows for the consideration of bedrock in the study area as uniform. In addition, past work focusing on establishing the tectonic evolution at an Afar-wide scale (Acocella, 2010) assume the Stratoid to be mechanically homogeneous.

Therefore, we make the simplifying, first-order assumption that the bedrock through which the rivers incise is uniform, allowing the erodibility to be treated as effectively constant across all grabens. This approach isolates the tectonic controls on knickpoint generation and enables comparison of knickpoint ages across the multiple kilometer-scale grabens. This assumption is also well supported by similar geomorphic studies in different tectonic and lithological settings across the globe (Densmore et al., 2003; Gasparini & Whipple, 2014; Harkins et al., 2007; Kobor & Roering, 2004; Stucky de Quay et al., 2019), where the aim is to extract and quantify tectonic signals on landscape evolution. These studies show that although bedrock erodibility can vary locally, a uniform erodibility model reliably recovers tectonic controls. Following this simple but effective approach gives us a robust and internally consistent framework for estimating fault initiation timescales across the study area.

In addition, the Afar Depression has remained persistently arid since at least the late Pleistocene, as evidenced by past work on paleoclimate reconstructions and isotopic records (Levin et al., 2004; Rime et al., 2023; Smail et al., 2025; Trauth et al., 2005). Moreover, studies have also demonstrated frequent oscillations in climatic conditions associated with multiple glacial-interglacial cycles and marine isotope stages that occur over short timescales of at the scale of 10^3–10^4 years (Tierney et al., 2017), which is considerably shorter than the ~2.0 Ma landscape evolution window analyzed in this study. Therefore, the local variations in climate and humid intervals are integrated over the 10^6-year period relevant to our study.

We assume that the faulting post-dated the emplacement of the Stratoid Series because presently, the rivers are located at the top of the footwall of the main graben bounding faults and are incising into these bedrock units (Figure 3b). Following this, the minimum erosion rate where the river crosses the fault (the catchment outlet) was estimated as follows:

$$\text{min. erosion rate}, E\ (m/yr) = \frac{H}{T} \tag{3}$$

Where H = Fault relief where the river crosses the fault in meters; and T = age of the bedrock at the top of the footwall, in years (ages of the Stratoid series from Tortelli et al., 2025a, Tortelli et al., 2025b) (Figure 2b).

To quantify the timescale of the landscape response to fault-induced uplift, we employed the unit stream power law (Tucker & Whipple, 2002; Whipple & Tucker, 1999). This equation expresses erosion rate (E) as function of the catchment drainage area (A, m^2) and the channel slope (S).

$$E = KA^m S^n \tag{4}$$

where the constant of proportionality, K, is the bedrock erodibility, an inherent property of the bedrock defining its erosional efficiency. Within the stream power law framework, the value of K is linked to the choice of the empirical exponents m and n, which in turn affects the scaling relationship between erosion and the channel drainage area and slope. It is important to note that the values of bedrock erodibility K, and the values chosen for m and n are interdependent. This means that varying the values for m and n can yield similar topographic fits but result in different calculated estimates for K (Harel et al., 2016; Royden & Taylor Perron, 2013; Smith & Fox, 2024; Stock & Montgomery, 1999). Sembroni et al. (2016) conducted a geomorphic characterization of two river systems draining the Ethiopian Plateau escarpment into the Afar Depression (Figure 1b), where incision occurs through basalt and the rivers appear to be in steady state. Using slope-area analysis and power-law scaling of river profiles, they estimated the channel concavity index ($m/n = \Theta$) ranging from 0.45 to 0.65, giving a mean concavity of these rivers to be 0.5. Additionally, other theoretical models, as well as past studies, focussed on rivers undergoing transient response to tectonic forcing have shown that m tends to fall within a narrow range of 0.4–0.6 and using $m = 0.5$ tends to be useful in comparing landscape responses across multiple catchments (Gasparini & Brandon, 2011; Harel et al., 2016; Kirby & Whipple, 2012; Mitchell & Yanites, 2019; Whipple & Tucker, 1999). In this study, we have chosen a unit stream power model where $n = 1$, and we explore a range of m values from 0.3 to 0.7, spanning the range of concavities estimated by Sembroni et al. (2016), (see below). The assumption of $n = 1$ has been shown in various past studies to be broadly appropriate for rivers incising through bedrock, particularly in regions undergoing active uplift and transient adjustment (D'Arcy & Whittaker, 2014; Royden & Taylor Perron, 2013; Quye-Sawyer et al., 2021). In addition, assuming $n = 1$ allows for consistent comparisons with the cosmogenic nuclide-based erodibility analysis conducted by Polun et al. (2024). They estimate K for just two catchments in the Dobi Graben and calibrate their results against a simple knickpoint migration model. Throughout the study area, there is a limited availability of other cosmogenic erosion rate data sets and spatially continuous lithology and erodibility constraints, so we make the simplifying choice of $n = 1$, to effectively compare knickpoint generation timescales across the study area in the case where calibration of other stream power parameters is not feasible.

We calculate different estimates of K using five m values from 0.3 to 0.7 in Equation 4. The resulting values of K therefore come from different versions of the stream power law and have different units. Following this, we also compute the ages of knickpoint formation from the respective value of K, and present results from both calculations in the Supporting Information S1, Table S1. But we choose $m = 0.5$ for the main purpose of our study, because this value (a) aligns with regional geomorphic constraints (Sembroni et al., 2016) (b) allows us to estimate K and model our knickpoint propagation to first-order (Kirby & Whipple, 2012; Pechlivanidou et al., 2019; Whipple & Tucker, 1999; Zhou et al., 2024) and (c) enables a direct comparison of our results with past K estimates in the Dobi Graben by Polun et al. (2024) and with other studies around the world.

Our chosen values reflect a simple stream power law approach and follow the methods used for transient landscapes around the world given we have relatively few constraints in this region to justify a more complex erosion law (Duvall et al., 2004; Gailleton, Mudd, et al., 2021; Leonard et al., 2023). We revisit the potential implications on bedrock erodibility estimates of choosing different m and n values, and further comparisons, in Section 5.1.

In principle, an erosion rate calculated at the fault (using Equation 3) can be used in the stream power law (Equation 4), and with measures of drainage area and channel slope to estimate the maximum values of bedrock erodibility of the basalt in units of yr^{-1}.

To constrain the bedrock erodibility (K) values, we selected catchments R13 and R14 within the Dobi Graben (Figure 3), because the published age ranges of approximately 1.5–2.0 Ma for the Afar Stratoid series are available for this region (Figure 2b), capture the variability associated different flows and stratigraphic units (Lahitte et al., 2003; Tortelli et al., 2025a, Tortelli et al., 2025b). We therefore use the bounding ages of 1.5 Ma and 2.0 Ma for R13 and R14 respectively, ensuring that the resulting K values derived from Equations 3 and 4, assuming the Afar Stratoid likely represents a homogeneous datum, and incorporate the full range of reported ages and uncertainties. These erodibility values represent reliable, first-order estimates calculated directly from available geochronological data, and they are further supported by independent, field-based geochemical K estimates of the same catchments from Polun et al. (2024). We also estimate different K values by varying m from 0.3 to 0.7 (therefore, using different stream power law frameworks) and present these results in the Supporting Information S1, Table S1.

The resulting erodibility values for catchments R13 and R14 (Figure 3a) were then applied to estimate, where present, the knickpoint formation ages in the other catchments, allowing for consistent temporal comparisons across the region. Using these estimates of bedrock erodibility, the knickpoint retreat velocity was calculated at each point along the trunk channel, based on the simple unit stream power law.

The unit stream power law represents an advective equation that implicitly defines a relationship between knickpoint retreat velocity and catchment drainage area, derived from partial differential formulations (Royden & Taylor Perron, 2013). This relationship is expressed as

$$V = KA^m S^{n-1} \quad (5)$$

When $n = 1$, the equation simplifies to show that the upstream migration velocity of the erosional wave, that is, the knickpoint retreat rate, scales directly as a function of catchment drainage area. In addition, there is a trade-off between the values of K and m for a unit stream power model, that is, varying m influences the absolute value of K, but the resulting knickpoint propagation rates and timescales are almost identical. We present these values in the Supporting Information S1, Table S1, and discuss them in Section 5.3.

Retreat rates were computed at each of the extracted points along the channel trunk. An iterative approach was then applied to estimate the time required for the knickpoint to migrate upstream from the outlet to its current position, following the methodology employed by Zondervan et al. (2020).

The estimate of the time taken for a knickpoint to have propagated to its current position was interpreted as the age of knickpoint formation. This procedure was repeated for both K values to produce two knickpoint age estimates for each catchment; and the range of ages produced thus encompassed the uncertainty in the erosion rate and knickpoint height estimates, as well as the margin of error in the published ages (Lahitte et al., 2003; Tortelli et al., 2025a, Tortelli et al., 2025b).

To investigate the spatial variation in ages of knickpoint formation, the resulting ages from the iterative approach outlined above, for each value of K, were plotted across the seven grabens from south-north (Afar scale trend in ages), and within each graben from E-SE to W-NW (local and graben-scale trends, if any).

3.3. Structural and Topographic Analysis

For the main graben bounding faults (Figure 4a), cross-strike (perpendicular to fault strike) swath profiles were extracted using the SWATHobj function in TopoToolbox. The profiles were extracted for 1 km wide sections, at 1 km intervals all along the fault. From each profile, the fault relief at that location was measured by subtracting the elevation of the base of the footwall from the elevation of the top of the footwall (in m). In the presence of any fan deposits on the graben floor, the base of the footwall was taken to be top of the fan deposit. The relief measured at each location was plotted against the distance along fault strike (in km) to obtain an along strike fault footwall relief profile. The along-strike profile traces are highlighted as shaded rectangles in Figures 4b–4e. The standard deviation values of the fault relief were used as the error estimates.

A similar approach was applied to any interacting segments and relay ramps; their respective fault reliefs were added to the main footwall relief profile to examine the interaction between the various fault segments.

The vertical height of the knickpoints above the footwall of each graben-bounding fault ($H_{\text{kp-fw}}$) was calculated by subtracting the elevation of the base of the footwall (H_b) from the absolute elevation of the knickpoints (H_{kp}).

$$H_{kp-fw} = H_{kp} - H_b \quad (6)$$

An empirically derived error of ±10% was added to these values to account for observational uncertainty in ascertaining the exact location and elevation of the knickpoint on the river long profile from the DEM. These values were then added to the fault/footwall relief profiles at their respective locations along strike, to study the temporal relationship between the ages of fault initiation and the formation of the knickpoints.

To better understand the age relationships of these graben systems in terms of their footwall reliefs (scales), we estimate the apparent throw rate, in mm/yr, on the footwalls of the major graben bounding faults (the vertical/uplift component),

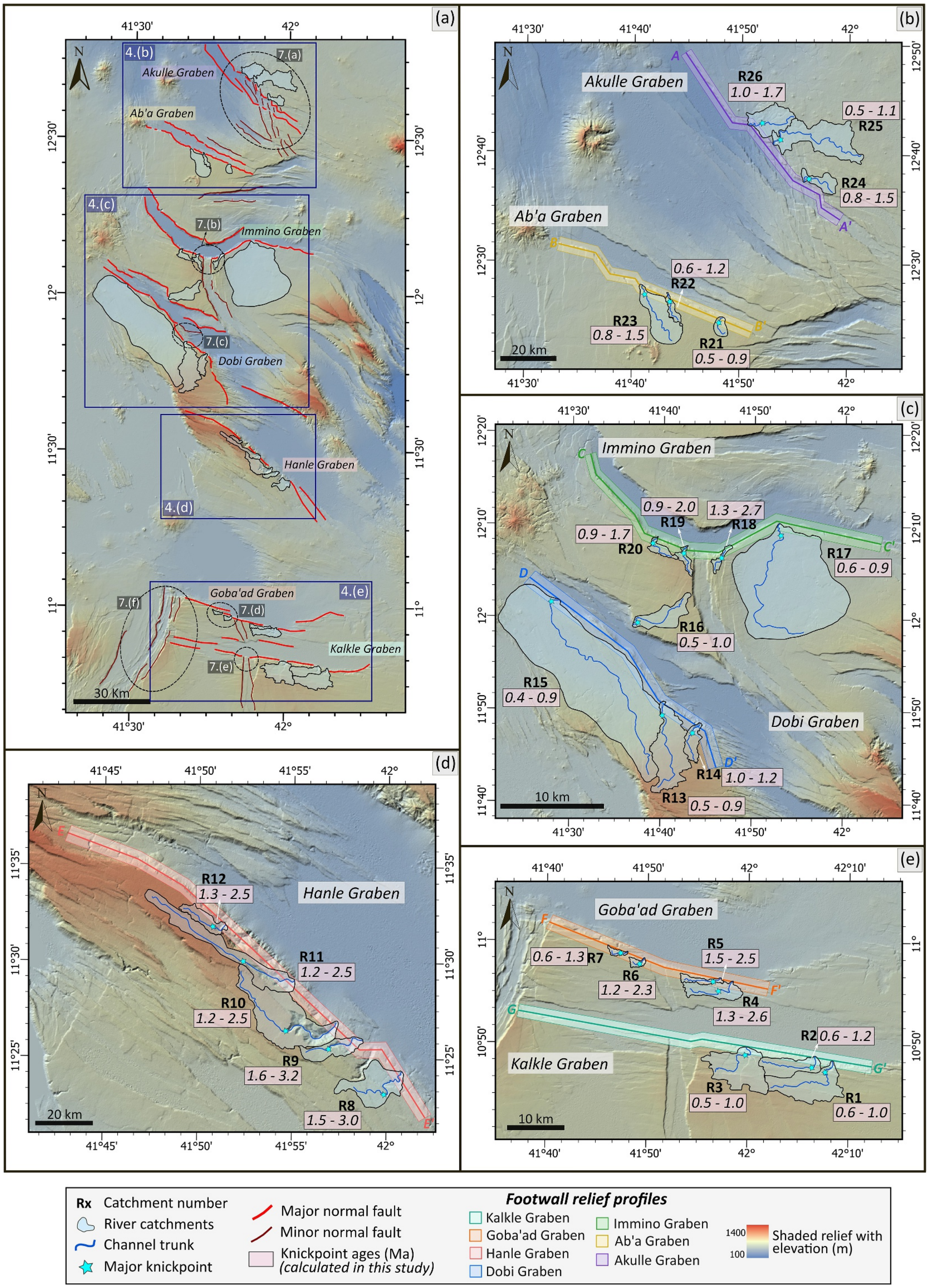
(a)
4.(b)
Akulle Graben
Ab'a Graben
7.(a)
4.(c)
7.(b)
Immino Graben
7.(c)
Dobi Graben
Hanle Graben
4.(d)
Goba'ad Graben
4.(e)
7.(f)
7.(d)
Kalkle Graben
7.(e)
30 Km
(b)
Akulle Graben
R26
1.0 - 1.7
0.5 - 1.1
R25
R24
0.8 - 1.5
Ab'a Graben
0.6 - 1.2
R22
R23
0.8 - 1.5
R21
0.5 - 0.9
20 km
(c)
Immino Graben
0.9 - 2.0
1.3 - 2.7
R19
R18
0.9 - 1.7
R20
R17
0.6 - 0.9
R16
0.5 - 1.0
R15
0.4 - 0.9
Dobi Graben
R14
1.0 - 1.2
R13
0.5 - 0.9
10 km
(d)
R12
1.3 - 2.5
Hanle Graben
R11
1.2 - 2.5
R10
1.2 - 2.5
R9
1.6 - 3.2
R8
1.5 - 3.0
20 km
(e)
Goba'ad Graben
R5
1.5 - 2.5
0.6 - 1.3
R7
R6
1.2 - 2.3
R4
1.3 - 2.6
R2
0.6 - 1.2
Kalkle Graben
R3
0.5 - 1.0
R1
0.6 - 1.0
10 km
Rx Catchment number
River catchments
Channel trunk
Major knickpoint
Major normal fault
Minor normal fault
Knickpoint ages (Ma)
(calculated in this study)
Footwall relief profiles
Kalkle Graben
Goba'ad Graben
Hanle Graben
Dobi Graben
Immino Graben
Ab'a Graben
Akulle Graben
1400
100
Shaded relief with elevation (m)

Figure 4.

$$\text{Throw rate} = \frac{H_{kp-fw}}{T_{kp}} \tag{7}$$

Where $H_{\text{kp-fw}}$ is the vertical height of the knickpoint above the footwall (in millimeters, from Equation 6), and T_{kp} is the age of knickpoint generation calculated in this study (in years). The obtained range of throw rates for each catchment reflect the error estimates in the ages of knickpoint generation.

4. Results

The seven graben systems analyzed in this study, from North to South in the Afar Depression—Akulle, Ab'a, Immino, Dobi, Hanle, Goba'ad and Kalkle, are bound by major normal fault segments, and are shown in Figure 4. These grabens exhibit broadly similar geometries, spanning 30–60 km in length and 7–10 km in width. From these, the Akulle, Ab'a, Dobi and Hanle grabens trend NW-SE, while the Goba'ad and Kalkle grabens trend E-W. The Immino graben displays an arcuate geometry, with the western half of the fault segment trending more NW-SE, and gradually transitioning to an E-W trend towards the eastern end (Figure 4c). The 26 catchments delineated and used in this study were grouped according to their respective graben systems. Catchments R1-R3 cross the main graben bounding fault in the Kalkle Graben (Figure 4e), similarly R4–R7 in the Goba'ad Graben (Figure 4e), R8–R12 in the Hanle Graben (Figure 4d), R13–R16 in the Dobi Graben (Figure 4c), R17–R20 (Figure 4c), R21–R23 in the Ab'a Graben (Figure 4b) and finally R24–R26 in the Akulle Graben (Figure 4b). The spatial distribution of these catchments and the major normal faults they cross and incise are highlighted in Figure 4a. Major knickpoints identified within each catchment are marked along the channel trunk (blue stars, Figures 4b–4e). The knickpoint formation age ranges calculated in this study are annotated on the map (pink boxes). All estimates of fault relief, knickpoint heights above fault, knickpoint ages and throw rates derived and calculated in this study are presented in Table 1.

4.1. Long Profiles and Footwall Relief

The normalized river long profiles of all 26 catchments are convex-up, with the presence of knickpoints despite the broadly homogeneous bedrock (Figure 5). Most profiles cluster around a common trend, displaying the knickpoints within a normalized elevation range of 0.6–0.9, and around normalized downstream distances of 0.6–0.8. The river long profiles of catchments R15 (Figures 4c and 5d) and R17 Figures 4c and 5e, show a deviation from this trend, with the knickpoints located at elevation values of 0.2–0.4, and a more concave-up geometry upstream of the knickpoint. Given the broadly homogeneous bedrock, these observations clearly indicate that all the rivers are undergoing a transient response to the fault activity in the Afar Depression. Consequently, our interpretation is that the rivers are actively recording and reflecting temporal fault evolution patterns in the timescale and locus of knickpoint migration upstream.

The seven footwall relief profiles of the main graben bounding normal faults are shown in Figure 6, and their respective profile traces are color-coded and marked on the map in Figures 4b–4e. Broadly, all profiles follow a bell-shaped relief profile, with the highest footwall relief towards the center of the fault segment, gradually decreasing towards the fault tips. In the northernmost section of the study area, the Akulle Graben (Figure 6a) shows a maximum footwall relief of 250m over a length scale of 45 km, and towards the SE section of the profile, the local variations in footwall relief are due to the presence of a second set of younger normal faults trending more N-S, cross-cutting the main graben fault that trends NW-SE (Figures 4a and 7a). In the Ab'a Graben (Figure 4b), the footwall relief reaches a maximum of 350m closer to the center of the 30 km long fault segment

Figure 4. (a) Regional overview map of the study area, showing the seven graben systems, and the locations of the major normal fault segments in the region (red) and the minor/cross-cutting normal fault traces (dark red). The 26 major river catchments analyzed in this study are delineated. The inset rectangles indicate the locations of the zoomed in panels (b–e), each focusing on specific grabens and their associated catchments. All data are displayed over a shaded relief and elevation map derived from the 30m DEM in ArcGIS Pro. The circular inset markers (7.a-f) correspond to the respective labeled panels in Figures 7b–7e Enlarged-view panels corresponding to the inset areas in (a), illustrating the numbered catchments, main channel trunk within each catchment, locations of the major tectonic knickpoints and the knickpoint formation ages calculated in this study. The shaded rectangles denote the along fault-strike footwall relief profile traces for each graben. (b) Akulle and Ab'a grabens (northern Afar Depression); (c) Immino and Dobi grabens (central Afar Depression); (d) Hanle graben (central Afar Depression); (e) Goba'ad and Kalkle grabens (southern Afar Depression). A consistent color scheme is applied throughout this study, with each graben represented by a distinct color across all figures, as shown in the legends, to facilitate visual continuity and comparison—Akulle (purple); Ab'a (yellow); Immino (green); Dobi (blue); Hanle (red); Goba'ad (orange) and Kalkle (teal).

Table 1

Summary of Key Results for Each Catchment Analyzed in the Study, Including the Absolute Elevation of the Knickpoints (m), Mean Footwall Relief (m), Height of Knickpoints Above the Footwall (m), Minimum and Maximum Estimated Ages of Knickpoint Formation (Ma), and Corresponding Minimum and Maximum Throw Rates (mm/yr)

Graben	Catchment number	Knickpoint elevation (m)	Mean footwall relief (m)	Minimum knickpoint age (Ma), from $K = 1.12 \times 10^{-6}$	Maximum knickpoint age (Ma), from $K = 5.67 \times 10^{-7}$	Knickpoint height above footwall relief (m)	Maximum throw rate (mm/yr)	Minimum throw rate (mm/yr)
Kalkle	R1	723	280	0.6	1.0	241	0.40	0.24
	R2	703	230	0.6	1.2	243	0.41	0.20
	R3	701	220	0.5	1.0	263	0.53	0.26
Goba'ad	R4	464	110	1.3	2.6	169	0.13	0.07
	R5	511	120	1.5	2.5	221	0.15	0.09
	R6	637	300	1.2	2.3	292	0.24	0.13
	R7	626	245	0.6	1.3	191	0.32	0.15
Hanle	R8	591	200	1.5	3.0	356	0.24	0.12
	R9	703	435	1.6	3.2	408	0.26	0.13
	R10	864	405	1.2	2.5	459	0.38	0.18
	R11	952	730	1.2	2.5	712	0.59	0.28
	R12	1,081	700	1.3	2.5	711	0.55	0.28
Dobi	R13	722	570	0.5	0.9	352	0.70	0.39
	R14	846	275	1.0	1.2	616	0.62	0.51
	R15	365	260	0.4	0.9	165	0.41	0.18
	R16	686	340	0.5	1.0	366	0.73	0.37
Immino	R17	346	215	0.6	0.9	146	0.24	0.16
	R18	614	515	1.3	2.7	494	0.38	0.18
	R19	684	570	0.9	2.0	579	0.64	0.29
	R20	725	600	0.9	1.7	600	0.67	0.35
Ab'a	R21	720	250	0.5	0.9	250	0.50	0.28
	R22	640	305	0.6	1.2	300	0.50	0.25
	R23	575	315	0.8	1.5	320	0.40	0.21
Akulle	R24	250	200	0.8	1.5	150	0.19	0.10
	R25	202	180	0.5	1.1	202	0.40	0.18
	R26	205	150	1.0	1.7	205	0.21	0.12

Note. These values underpin graphical analyses and data presented in Figures 5, 6, 8, 9 and 10.

(Figure 6b). The Immino Graben (Figure 4c) fault segment spans 65 km and the footwall relief reaches a maximum 650m (Figure 6c). Around 23 km along fault strike of the roughly E-W striking Immino Graben, there is a local topographic low which highlights a smaller scale cross-cutting graben system, trending N-S (Figure 7b). Rivers R18 and R19 cross the main graben bounding fault in Immino Graben, and the knickpoints formed upstream of the fault are marked, highlighting the prominent incised canyons in 3D. The Dobi Graben, in the center of the Afar Depression (Figure 4c) reaches a similar footwall high of 650m over a shorter fault length of 45 km (Figure 6d). An additional feature in the Dobi graben is the ~7 km long minor fault segment, intersecting the main graben bounding fault at ~20 km along fault strike (Figure 7c). R13 in the Dobi Graben shows pronounced incision in the form of a deep canyon, and a major knickpoint was identified at the top of this canyon (Figure 7c). The Hanle Graben (Figure 4d) has the highest fault relief, with a maximum of 900m across the short 25 km fault segment (Figure 6e). Moving further south in the study area, the Goba'ad and Kalkle Grabens (Figure 4e), trend E-W, and the western ends of the graben are located proximal to the axis of the Northern Main Ethiopian Rift segment (Figures 1 and 7f), and the main graben bounding fault reliefs are 500m (Figure 6f) and 300m (Figure 6g), respectively, at the eastern fault tips. Other than this variation, the Goba'ad Graben follows the broad bell-shaped profile trend, with the relief decreasing from 400m in the center of the fault segment to 100m at the

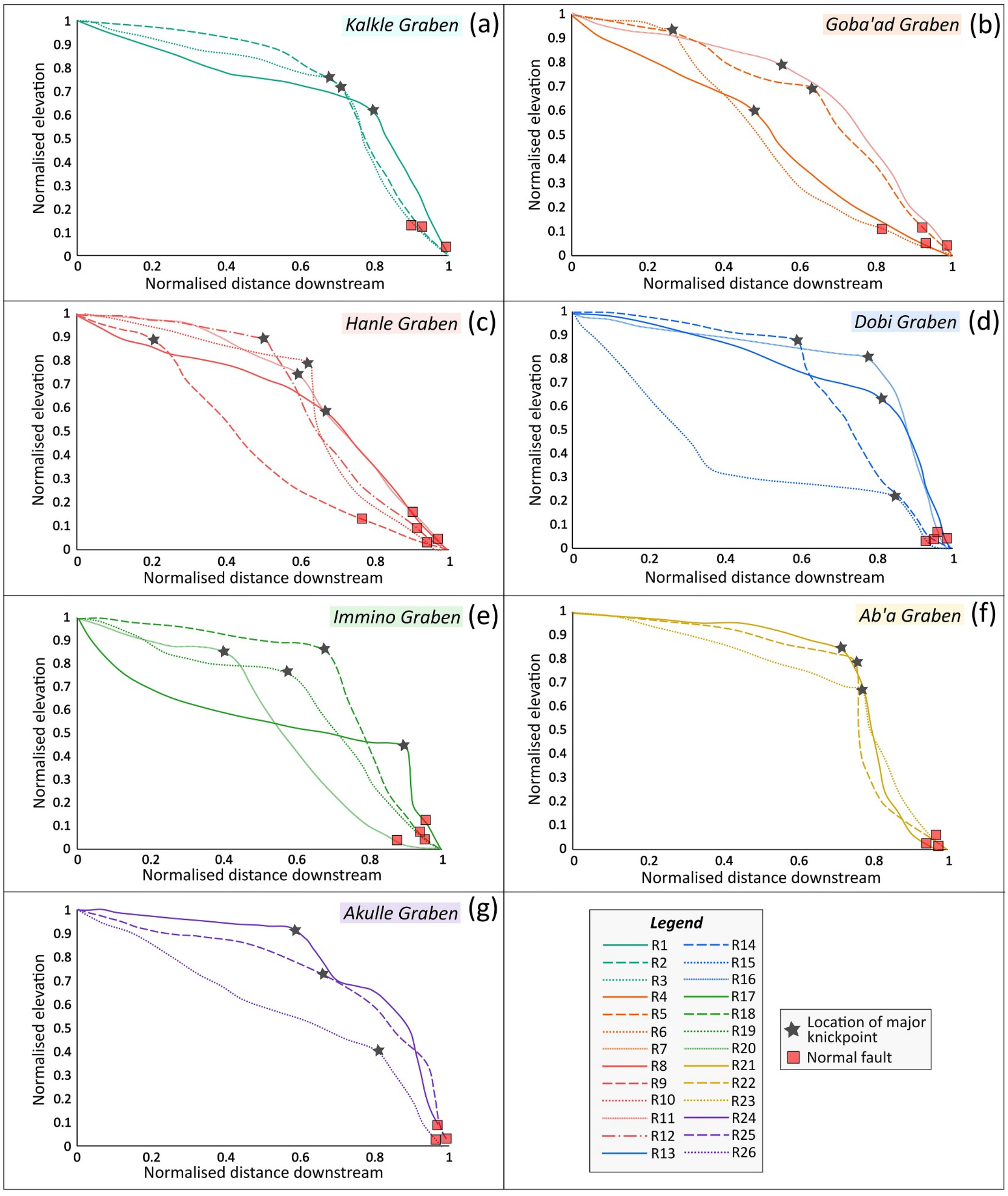

Figure 5. Normalized River long profiles for the 26 rivers in the study, (grouped by graben). Normalized distance and elevation values derived from Equations 1 and 2, respectively. The locations where the river intersects the normal fault plane (red squares) and the location of the tectonic knickpoint (stars) are marked. The catchment locations for each of the rivers are shown in Figures 4b–4e. (a) Kalkle Graben, R1–R3; (b) Goba'ad Graben, R4–R7; (c) Hanle Graben, R8–R12; (d) Dobi Graben, R13–R16; (e) Immino Graben, R17–R20; (f) Ab'a Graben, R21–R23; (g) Akulle Graben, R24–R26.

western fault tip (Figure 6f). A clear interaction between the minor fault segment in Goba'ad Graben and R7 is observed in 3D view in Figure 7d. R7 visibly incises through the relay ramp created as such, and the knickpoint formed on the footwall is marked. River R6 has a similar catchment size to R7 and has formed a knickpoint at the top of the incised section (Figures 4e and 7d), but flows across the main graben bounding fault. On the other hand, the Kalkle Graben exhibits a slightly different relief profile, with a topographic low at 16 km along strike (Figures 6g and 7e) due to the intersection of a smaller-scale perpendicular graben system that is roughly parallel to the main NMER segment (Figures 7e and 7f). Overall, the data in Figure 6 suggests that the majority of knickpoints plot on the footwall crests in terms of elevation, within error.

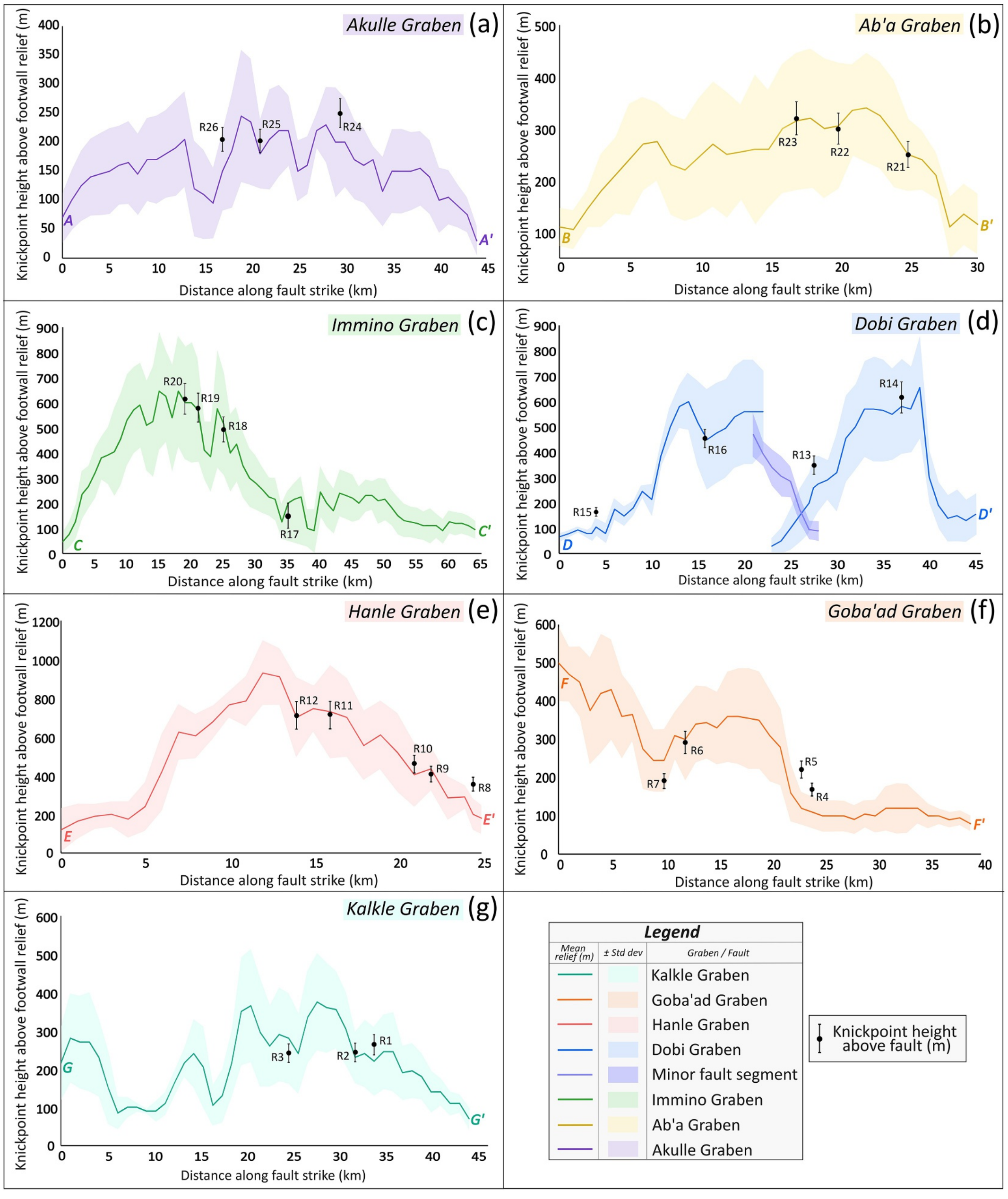

Figure 6. Footwall relief profiles for each of the seven grabens analyzed in this study, shown in individual panels. Each profile represents the footwall relief extracted along the fault strike, with the solid line indicating mean elevation and the shaded envelope is the +/− standard deviation. The heights of the knickpoints above the fault footwall relief are shown as black circles. An error of +/− 10% was added to account for the uncertainty in accurate estimations of the knickpoint location. Profile traces correspond to the shaded fault-trace rectangles in Figures 4b–4e.

To test this relationship explicitly, we plotted the heights of the knickpoints above the footwall relief (meters) against the footwall relief of the main graben bounding fault at that point (meters) (Figure 8). This graph shows that the knickpoint height is directly related to the footwall relief by a linear relationship—the line of best fit (with the y intercept set to 0) plotted for the data set can be represented by an r^2 value of 0.9804, and the equation $y = 1.03X$ (Figure 8), meaning that the gradient of this line is ca. 1. This result confirms that the knickpoints were generally created as a result of the initiation and growth of the main fault segment on which they lie, therefore tracking the timing of fault initiation, and most do not relate to later linkage (c.f. Whittaker & Walker, 2015). While the knickpoints predominantly track fault initiation, a few exceptions point towards more localized trends.

10.1029/2025TC009276

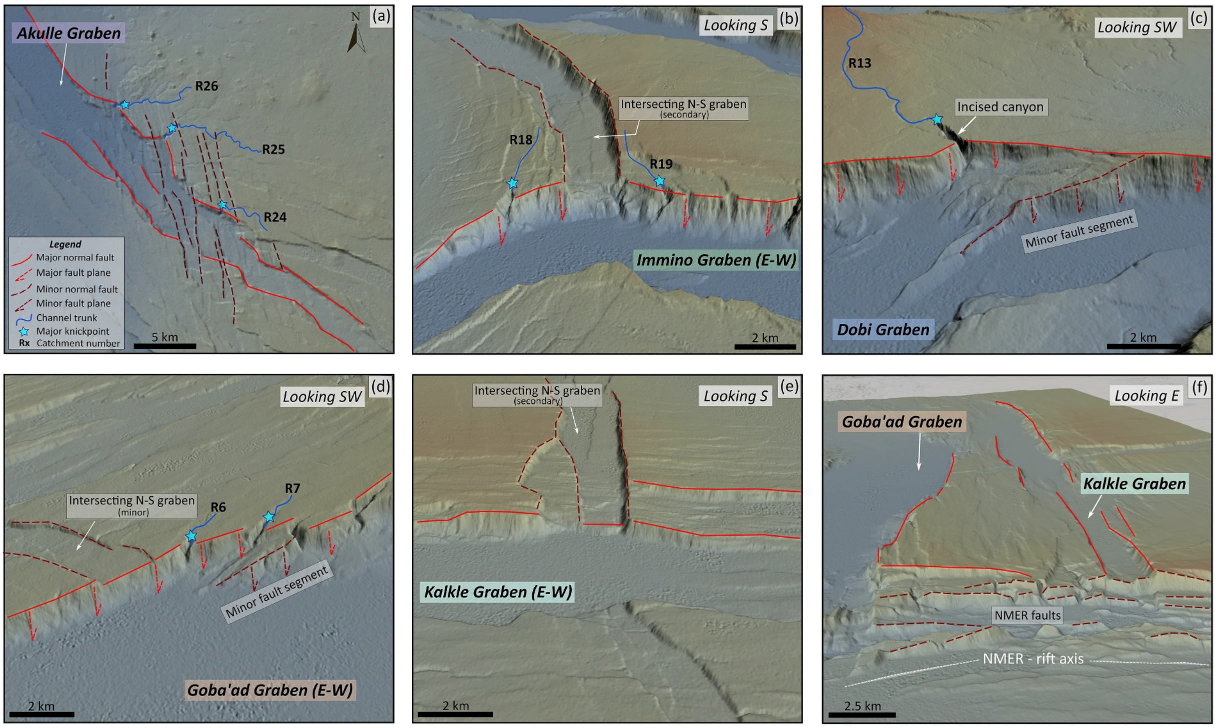

Figure 7. Locations of all panels correspond to the circular inset markers in Figure 4a. (a) Bird's eye view of the interacting normal fault systems in the Akulle Graben showing the main graben bounding normal faults (red) crosscut by minor intersecting faults (dark red, dashed) (b)—(f) 3D perspective view sections extracted from the Local Scene—Map 3D View setting in ArcGIS Pro, with 3X vertical exaggeration to enhance structural contrast. The panels highlight key fault geometries across the study area including cross-cutting grabens and intersecting fault segments. Where present, the main channel trunks and the major knickpoints are marked, emphasizing the incision and drainage response to faulting. (b) Secondary, perpendicular graben intersecting the main Immino Graben. (c) Minor fault segment intersecting the Dobi Graben, corresponding to the violet secondary profile in Figure 6d. (d) Minor fault segment intersecting the Goba'ad Graben, proximal to the outlet of catchment R7. (e) Secondary, perpendicular graben intersecting the main Kalkle Graben. (f) Interaction zone between the Goba'ad and Kalkle Grabens and the axis of the Northern Main Ethiopian Rift (NMER).

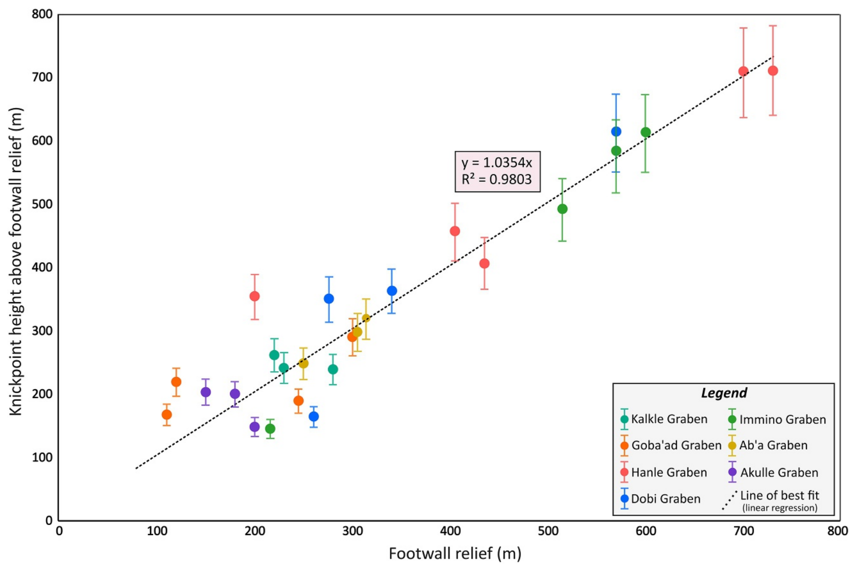

Figure 8. Plot of the knickpoint height above the fault footwall relief against the extracted footwall relief. An error of ±10% was added to account for the uncertainty in accurate estimations of the knickpoint location. The black-dotted line represents the line of best-fit, the linear regression, with the equation of the line in the pink box.

In cases where the knickpoint plots below the footwall relief, as for R7 in the Gobaad graben, we interpret that the river is responding to a younger tectonic feature such as a cross-cutting, minor fault segment (Figure 7d). Similarly, for knickpoints plotting above the footwall crests, such as R4 and R5 in the Goba'ad Graben, we interpret that they were formed during the early stages of fault initiation before the growth of present-day footwall relief, potentially representing older secondary tectonic signals relative to the dominant population of knickpoints plotting on the footwall crest.

4.2. Bedrock Erodibility, Knickpoint Analysis and Fault Initiation

In catchments R13 and R14 of the Dobi Graben (Figures 2b, 3, 4c), the amount of incision was found to be approximately 500 and 640m, for channel slopes of ~0.06 and drainage areas of 86.5 and 15.5 km^2, respectively. From these incision and geomorphic metrics, the values of bedrock erodibilities (K) for the Afar Stratoid series were calculated in this study to be 5.67×10^{-7} yr^{-1} from R13 and 1.12×10^{-6} yr^{-1} from R14. The bedrock sections underlying each catchment are grouped under the Upper Stratoid series and have been independently dated to 1.5 ± 0.06 Ma and 2.0 ± 0.06 Ma, proximal to R13 and R14, respectively (Lahitte et al., 2003; Tortelli et al., 2025a, Tortelli et al., 2025b). These values cover the range of bedrock ages reported for the wider Dobi Graben (Figure 2b) and helped better constrain the uncertainty in the timing of incision and knickpoint formation.

Consequently, the knickpoint formation age estimates for each of these rivers range from 0.5–0.9 Ma in R13 and 1.0–1.2 Ma in R14. Based on this, we obtained knickpoint propagation upstream rates of 0.27–0.32 mm/yr in the Dobi Graben since fault initiation.

Following this approach for the other river systems in the study area, using bedrock erodibilities derived above from Equation 4, the range of ages for knickpoint formation in each catchment was calculated (Figures 4b–4e). In correlation with the knickpoints plotting on the footwall crest from Figure 6 and the linear relationship between the footwall relief values and heights of the knickpoints above the footwall in Figure 8, we interpret in this study that the age of knickpoint formation is the maximum age of initiation of the main graben bounding faults. These values represent maximum estimates because K was derived using the available age constraints for the Stratoid Series (1.5–2.0 Ma; Figure 2b). As knickpoint formation must post-date basalt emplacement and associated fault initiation, the ages of knickpoint generation we present in our study define upper bounds and may be younger if incision began later.

Figure 9a shows the calculated knickpoint ages for all catchments, plotted by graben from SE-NW, and at the depression-scale from S-N. The rectangles in the figure represent the range of knickpoint ages derived using the two calibrated bedrock erodibility (K) values calculated for the representative catchments R13 and R14 (Figure 3a) in this study using Equation 4. These bounds bracket the possible regional variations in the erodibility of the Stratoid series, and provide maximum, conservative constraints on knickpoint formation ages across the region.

The graph highlights the spatial variation in knickpoint formation ages throughout the study area, with notable trends and deviations at the graben scale. The Kalkle Graben (teal rectangles, Figure 9a) in the South records knickpoint formation ages of 0.6–1.2 Ma. All three catchments in the Kalkle Graben have consistent age ranges. The Goba'ad Graben (orange rectangles, Figure 9a) overall is older than the Kalkle and exhibits a minor graben-scale variation in knickpoint ages. This corresponds to catchment R7, which is younger compared to the other catchments in the graben (R4, R5 and R6), with a knickpoint formation age of 0.6–1.2 Ma, while the others are older (1.0–2.5 Ma). From this age estimation and the map of major faults in the Afar Depression, this knickpoint is interpreted to be formed by uplift and incision caused by the formation and growth of the smaller interacting fault segment, forming a relay ramp with the main graben bounding fault (Figure 7d). The Hanle Graben (red rectangles, Figure 9a) records the oldest knickpoint ages, ranging from 1.0–3.0 Ma. The Dobi graben (blue rectangles, Figure 9a), located in the center of the depression, records knickpoint formation ages of 0.5–1.2 Ma, and with consistent age estimations throughout the graben, the Dobi Graben is one of the youngest normal fault systems in Afar. Moving further North, the Immino Graben (green rectangles, Figure 9a) also exhibits a graben-scale variation in ages. R17 at the eastern end of the main Immino fault segment is younger, with ages <1 Ma, and the knickpoint ages get older towards the central and western ends of the segment (1.0–2.5 Ma). The Ab'a Graben (yellow rectangles, Figure 9a) is younger than the Immino and the ages for these knickpoints were 0.6–1.5 Ma. Lastly, the Akulle Graben (purple rectangles, Figure 9a) in the northernmost end of the study area is structurally complex with two sets of normal faults—the main graben bounding fault system trending NW-SE, and a second set trending more N-S (Figure 7a). The 3 identified catchments in this graben interact with different segments;

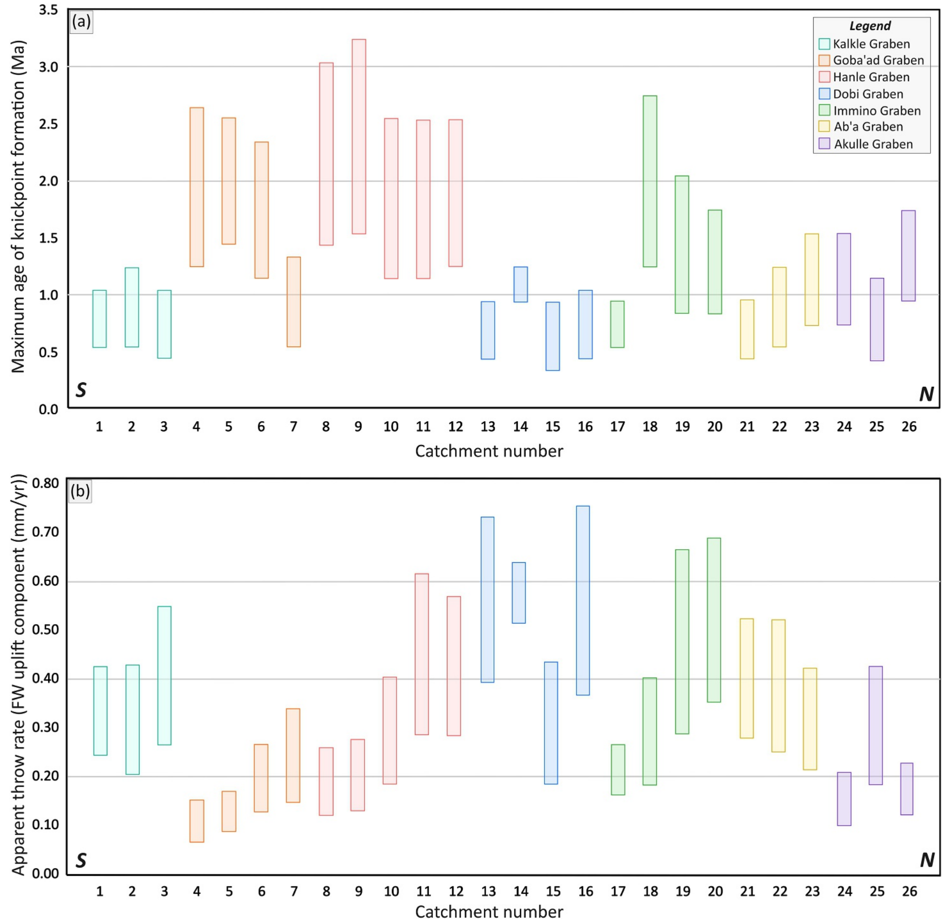

Figure 9. Plots of (a) Maximum knickpoint formation ages in each catchment (in Ma); and (b) Minimum fault throw rates (mm/yr), representing the footwall uplift component Data are plotted for each catchment, grouped by graben, from South to North. In (a), each shaded rectangle represents the age range derived from the two bedrock erodibility (*K*) values calculated in this study. The upper and lower bounds correspond to the maximum ages associated with each *K* value, providing a visual representation of the uncertainty in the estimation of knickpoint migration timescales. In (b), shaded rectangles represent the range of throw rates calculated from the two age estimates. The bounds correspond to rates derived from each age, reflecting the uncertainty in the calculation of the throw rates.

hence this graben also records varying ages. Catchment R25 was mapped to be intersecting the N-S set of faults, while catchments R24 and R26 intersect the main graben-bounding NW-SE fault. Thus, the younger ages in catchment R25 (0.6–1.1 Ma) indicate that the N-S trending fault system is younger than the main graben fault, supported by the older ages in R24 and R26 (0.8–1.8 Ma).

The throw rates for each catchment are plotted from S-N in the study area, in Figure 9b and the catchment numbers correspond to those in Figure 9a. The graph shows a clear increase in throw rates towards the center of the study area, underscoring a dominant regional pattern alongside local, graben-scale variations. The Kalkle normal fault shows a near consistent throw rates, ranging from 0.2–0.5 mm/yr. The Goba'ad graben shows an increase in throw rates from 0.1 mm/yr to 0.15–0.3 mm/yr towards the western end of the fault strand. The highest throw rate at R7 can be attributed to the younger intersecting fault segment (Figure 7d) and younger knickpoint age (Figure 9a). The Hanle Graben exhibits a similar trend of increasing throw rates, with notably higher overall values than the Goba'ad, from 0.1 to 0.2 mm/yr in the SE to 0.3–0.6 mm/yr in the NW (Figure 9b), towards the center of the depression (Figure 4d). In the center of the region, the Dobi Graben has the highest overall throw rates, ranging from 0.4 to 0.8 mm/yr. R15 has a relatively lower throw rate of 0.2–0.4 mm/yr (Figure 9b) due to its location at the NW fault tip (Figure 4c). Throw rates generally decrease towards the northern half of the study area. The Immino fault mirrors the trend observed in the Hanle and Goba'ad grabens, with rates increasing from 0.2 mm/yr at the western end to 0.3–0.65 mm/yr near the center of the fault segment (Figure 9b). The Ab'a fault shows a relatively consistent throw, ranging from 0.2 to 0.5 mm/yr. The Akulle Graben aligns with the overall trend in decreasing throw rates away from the center of the depression, with values of 0.1–0.2 mm/yr along the main graben bounding fault. The younger, intersecting fault (Figure 7a, 9a) displays moderately higher rates of 0.2–0.4 mm/yr.

5. Discussion

5.1. Landscape Response to the Fault Activity

Our results show that for all 26 catchments identified in the Afar Depression, there is one major knickpoint located upstream of the main graben bounding normal fault, at normalized elevations of 0.6–0.9 (Figure 5). From the DEM mapping (Figures 4b and 7) and the river long profiles (Figure 5), the convex-up profile with clear slope-break knickpoints and incised canyons imply that rivers are undergoing a transient response to the normal faulting and are still actively recording and reflecting the tectonic activity, clearly demonstrating the use of quantitative geomorphology as a suitable tool in studying and understanding fault activity in a magma-rich rift setting. Owing to the consideration of largely homogeneous bedrock in the study area (Rime et al., 2023) we discount a significant lithological effect on knickpoint generation. Additionally, the effects of climate on the incision and erosion of the river systems are also limited due to local, short-term climatic variations (10^3–10^4 years) (Levin et al., 2004; Tierney et al., 2017) that integrate over the 10^6-year timescales analyzed in this study, and the mostly dry and arid conditions since the Pleistocene (Gasse & Street, 1978). Seeing that the knickpoint heights plot nearly on the crest of the footwalls (Figure 6), we additionally conclude in this study that the knickpoints have formed with or just following the initiation of the main graben bounding fault on which they are located. Therefore, the formation of, and activity on the main graben bounding faults associated with the linkage between the Red Sea and Gulf of Aden rift segments is the main driver behind incision in the rivers and subsequently, the formation of the knickpoints.

We estimate in this study that the bedrock erodibility of the Afar Stratoid Basalt series ranges between $5.67 \times 10^{-7}\ \text{yr}^{-1} - 1.12 \times 10^{-6}\ \text{yr}^{-1}$, and this range accounts for the margin of error in the dated ages of the rock. This value was obtained using a simple model of the unit stream power law, where we chose $m = 0.5$ in Equation 4, which implies that the rate of erosion in the catchment scales with the square root of the catchment drainage area. Choosing $n = 1$ produces a linear scaling relationship between erosion rate and channel slope that is physically meaningful and does not suggest knickpoint generation by shockwave behavior (Berlin & Anderson, 2007; Pritchard et al., 2009; Roberts et al., 2012). We acknowledge that more complex models of the stream power law exist, with values of m varying from 0.3 to 0.6 and $n \neq 1$ (Gailleton, Sinclair, et al., 2021; Royden & Taylor Perron, 2013), but we have chosen a simpler model to balance interpretability, empirical relevance, and comparison of further analyzed data across the study area. Although varying exponent combinations, that is, different erosion law frameworks, produce different absolute values of K (and corresponding units), the resulting knickpoint retreat rates remain of comparable magnitude. We present a comparison of K values calculated using a range of m values ($m = 0.3$–0.7) in Table S1 in the Supporting Information S1. From this, we observe that while the choice of m results in a difference in the units and absolute magnitude of K, the estimated knickpoint formation ages differ only by a factor of $\pm 10\%$. Therefore, the velocity of knickpoint migration, and subsequently the formation ages are not substantially influenced by the value of m.

The unit stream power model chosen in this study allowed for direct comparisons with the independent estimates of erosion rates and bedrock erodibilities by Polun et al. (2024). Specifically, their analysis of the Dobi Graben catchments, corresponding to R13 and R14 in our study, yielded incision rates calibrated using terrestrial cosmogenic nuclide (TCN) analysis. Their TCN derived erosion rates were applied within the same stream power framework (with $n = 1$) we outline in Equation 4 to obtain K value estimates ranging from $8.88 \times 10^{-7}\ \text{yr}^{-1} - 2.65 \times 10^{-6}\ \text{yr}^{-1}$ reflecting timescales of 10^3–10^4 years. These values are comparable by order of magnitude to the K values we estimate over a longer temporal scale of 10^6 years, reinforcing our results and the use of the simple stream power model ($n = 1$). Additionally, it is important to note that we have not explicitly used channel width in our calculations or modeled discharge variation over time. A^m in Equations 4 and 5 therefore represents an integrated discharge component (c.f. Hack, 1957; Roberts et al., 2012; Whipple & Tucker, 2002). Considering that local and short-term (10^3–10^4 years; Tierney et al., 2017) variations in rainfall integrate over the 10^6-year timescales considered in this study, we discount a significant effect of rainfall on the erosion and generation of knickpoints. The rainfall would have to be changed by a large factor to change the value of K.

The erodibility values calculated in our study fall within the same orders of magnitude, as reported in other global studies using comparable stream power law frameworks and units. For a similar version of the stream power law applied over 10^6-year timescales, Stock and Montgomery (1999) also show erodibility values of 10^{-7}—10^{-6} yr^{-1} for various lithologies in Australia, Hawaii (basalt—volcaniclastics), California, and Japan. In the Central Apennines, Whittaker and Boulton (2012) found K values within 10^{-7}–10^{-6} yr^{-1} over 10^5–10^6-year timescales, while K estimates 10^{-6} yr^{-1} have been estimated in the Gediz and Hatay Graben systems in Turkey (Kent et al., 2017; Whittaker & Boulton, 2012) as well as in the Gulf of Corinth, Greece for rivers crossing active normal faults in a fault-dominated rift setting (Gallen & Fernández-Blanco, 2021; Pechlivanidou et al., 2019; Zhou et al., 2024). This highlights the consistency of our results with other established erosional behavior across global active tectonic settings.

5.2. Spatio-Temporal Evolution of the Graben Systems

The observable linear relationship between the heights of the knickpoints and the extracted footwall relief (Figure 8) shows that the knickpoints were primarily created due to the initiation and growth of main graben bounding faults and a small number reflect more localized tectonic influences. In particular, knickpoints associated with intersections between minor fault segments and the main graben fault may record younger phases of fault growth or propagation (for e.g., R7 in the Goba'ad Graben). Because these features are spatially discontinuous, we therefore suggest that the ages of knickpoint formation are a true reflection of the maximum graben initiation ages. Thus, the age ranges highlighted in Figures 4b–4e, 9a represent the overall timescales of initiation of the main graben bounding normal faults in the Afar Depression. The integration of geomorphic markers with fault relief mapping (Figures 6 and 8) and the differences in throw rates and graben scale (Figure 9b, Figure S1 in Supporting Informating S1) allowed us to infer a spatio-temporal fault initiation pattern. This approach contributes to a more refined understanding of fault evolution in the Afar Depression, and adds quantitative, structural based constraints on the current models of rift linkage.

We therefore present a landscape dynamics-based model of fault evolution grounded in the relative age relationships between the principal graben systems (Figure 10). This spatial framework reconstructs the relative sequence and timing of fault activity as derived from landscape dynamics, offering insights into how and when different graben segments were initiated and became tectonically active.

Between 3 and 2 Ma, the Afar Depression was dominated by the eruption of the Afar Stratoid Basalt series (Tortelli et al., 2025a, Tortelli et al., 2025b), and the initiation of the first major normal fault systems in Central Afar. Our age model indicates that the Hanle fault system initiated around 3 Ma, followed closely by the development of the central-western Immino fault at 2.7 Ma. Concurrently, extensional strain in southern Afar was accommodated by the formation of the Goba'ad basin around 2.5 Ma, which exhibits an E-W geometry (Figure 10a).

Between 2 and 1 Ma (Figure 10a), there was an increase in fault activity across the depression, marked by the initiation of the Ab'a and Akulle graben-bounding faults around 1.5 Ma. These structures strike parallel to the Dabbahu-Manda-Harraro (DMH) magmatic segment (Figure 1), and form part of the developing linkage zone between the RS and GoA rifts. In the southernmost extent of Central Afar, the Kalkle graben emerged in proximity to the northern axis of the MER. Its orientation and relatively higher throw rate suggest that it accommodates enhanced extension in the southern sector.

The Dobi graben fault system initiated around 1.0 Ma (Figure 10b), and rapidly evolved into the dominant extensional structure, as evidenced by its high throw rates reaching up to 0.8 mm/yr (Figure 9b). Around 1.0–0.9 Ma, the eastern segment of the Immino graben also developed (Figures 4c, 9a, 10b). Although this segment exhibits relatively low throw (R17, Figure 9b), its initiation allowed for the formation of the Immino graben's arcuate geometry. The progressive change in fault strike from NW-SE in the western segment to E-W in the eastern segment suggests structural reorientation associated with the rift linkage, which is indicative of active fault segment linkage between the RS and GoA rifts. This faulting coincides with the onset and propagation of the continental segments of the RS and GoA rift systems—the DMH and Asal magmatic segments (Acocella et al., 2008), suggesting that our fault initiation chronology (Figure 10) is consistent with the broader rift dynamics.

Evolution of the linkage between the three major rift systems has generated various minor normal faults that form grabens or crosscut the main graben systems. The age constraints we obtain in Figure 9a for the Akulle Graben

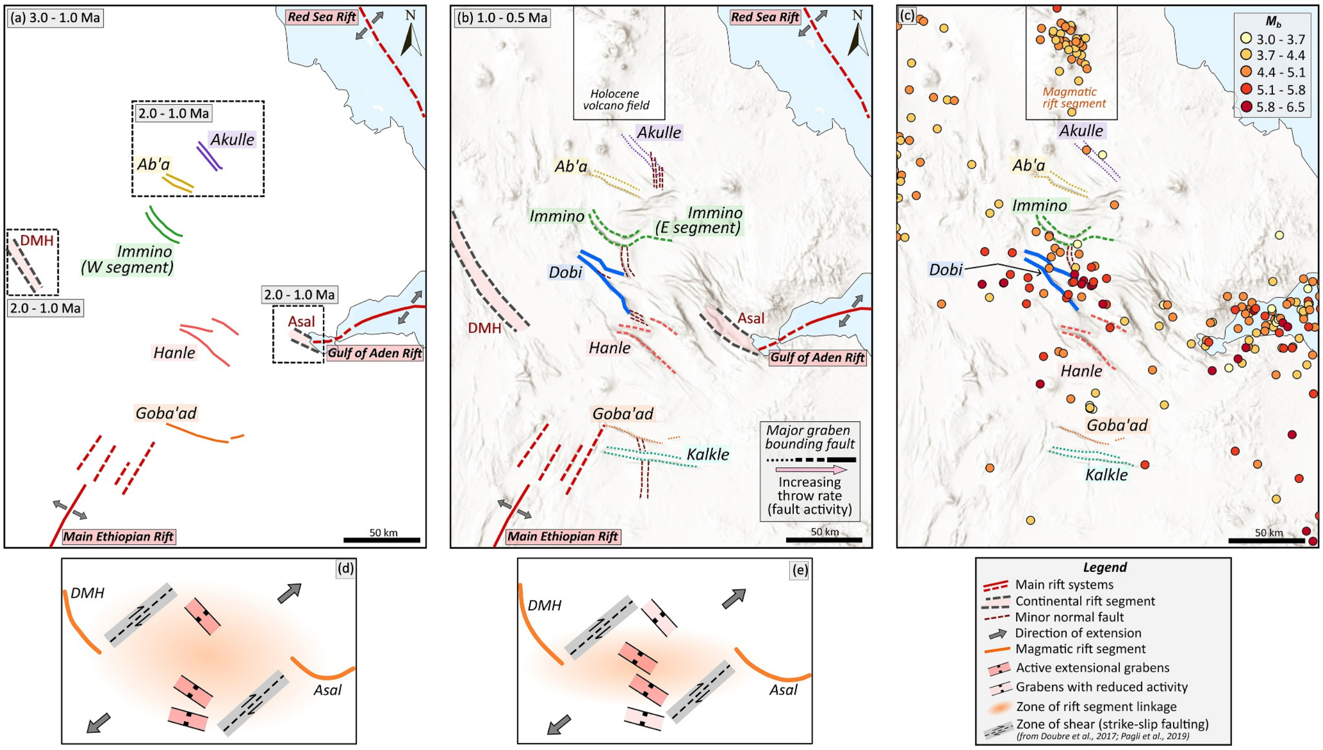

Figure 10. Schematic map-view diagram illustrating the spatio-temporal evolution of the major graben systems in Central Afar between 3.0–0.5 Ma, as determined from our geomorphic analyses. (a) Faults initiated between 3.0–2.0 Ma are shown across the map. The inset boxes highlight fault segment growth from 2.0–1.0 Ma (b)-(c) Data overlaid on a global terrain topography base layer. (b) Fault activity from 1.0-0.5 Ma, with fault traces dotted and weighted by throw rate—thicker line indicates higher throw rate. (c) Spatial distribution of earthquakes (≥3.0 Mb) extracted from the NEIC Seismicity catalog between 1900-present day. Concentration of earthquakes labeled with fault and magmatic segments to distinguish tectonic and volcanic contributions to seismicity. Data sourced from USGS (2025). (d) and (e) Conceptual sketches illustrating the inferred distribution of active deformation within the rift linkage zone during stages (a) and (b), respectively. These sketches represent the same geographical area shown in panels (a) and (b). The extensional grabens are based on the spatial patterns of fault initiation ages and throw rates derived in this study, shown in Panels (a–b), and the gray rectangles denote zones of strike-slip faulting, locations derived from (Doubre et al., 2017; Pagli et al., 2019).

(R25, Figure 4e) show that more N-S trending faults (Figures 4a and 7a) have initiated later, around 1–0.5 Ma (Figure 10b), which could be translated to the other minor perpendicular faults intersecting the Immino and Dobi grabens. Faults parallel to the axis of the MER (Figures 4a, 7e and 7f) would have also formed after the generation of the main graben basins, following the northward propagation of the NMER (Bonini et al., 2005; Wolfenden et al., 2005).

5.3. Regional Implications for Rift Linkage Mechanisms

The Afar Depression is structurally complex, with the fault segments playing an important role in accommodating the rift-related extension between the DMH and Asal magmatic segments (Acocella et al., 2008; Doubre et al., 2017; La Rosa et al., 2022; Muluneh et al., 2024; Pagli et al., 2014, 2019). Analysis of fault throw rates across the study area (Figure 9b) reveals spatial variability in the fault activity, indicating that the extension is accommodated to different degrees by the major grabens. Notably, the throw rates progressively increase towards the center of the linkage zone. Among the seven graben systems analyzed, the highest are concentrated in the central part of the depression, specifically between the Immino, Dobi and Hanle grabens; of these, the Dobi has the highest throw rates (Figure 9b). Consequently, we interpret that majority of the extension in Afar is localized at the center of the lateral step between the DMH and Asal magmatic segments (Figure 10e). The Dobi Graben has emerged as the dominant, active structure after 1 Ma, implying that most of the extension in Central Afar is localized at the Dobi. Both, the spatial distribution of seismicity from the earthquake catalog data (Figure 10c) and geodetic strain rates (La Rosa et al., 2022; Pagli et al., 2019) reveal a clear concentration of extensional strain in Central Afar, primarily near the Dobi graben, independently supporting our interpretation of Dobi as the principal locus of present-day deformation (Figure 10b; 10e). Our results complement the numerical modeling results produced by Muluneh et al. (2024), who have suggested that extension has progressively localized through time towards the center of rift step-over zone.

Figure S1 in Supporting Information S1 presents a scatter plot comparing fault initiation ages (Ma) with corresponding footwall relief (*m*) across the analyzed grabens. The data reveal a non-systematic relationship between these two parameters—older grabens do not consistently exhibit greater relief, nor do younger ones necessarily show lower topographic expression. When considered alongside Figure 9a, this pattern suggests that there is no definite correlation between graben scale and initiation age. This implies that the graben development in the central linkage zone is not synchronous; instead, grabens evolve progressively over time to accommodate the migrating extension. Our results confirm that the linkage in Central Afar has been active for at least 3 Ma and the normal fault-bound graben systems have formed as a result of the extension. From the graben age and throw rate relationships (Figure 9), we see that the fault activity in Central Afar is dynamic and migrates. Individual graben systems initiate, accommodate extension over 0.5–1 Ma timescales, and subsequently diminish in activity as the strain progressively transfers to adjacent fault systems (Figures 10a and 10b). Overall, we show that the strain has focused towards the center of the linkage zone (Figures 10d and 10e). Progressive fault activity migration and localization have been documented across the Edward-George, Luangwa, and Malawi branches of the East African Rift system, where fault activity increases as the rift evolves (Wedmore et al., 2022, 2024; Williams et al., 2022). Similar trends are observed in the Corinth Rift, Greece, where fault throw rates vary and strain rapidly localizes over time reflecting dynamic fault system evolution in response to ongoing extension (Nixon et al., 2016, 2024).

Our interpretation of fault linkage in Central Afar indicates that extension is primarily accommodated through the development of en-echelon normal faults. This structural style differs from the traditional model of bookshelf faulting (left-lateral strike-slip faults) previously proposed for Central Afar (e.g., Kidane et al., 2003; Manighetti et al., 1998, 2001; Muluneh et al., 2013). Illsley-Kemp et al. (2018) outlined a range of mechanisms for strain transfer and accommodation between linking rift segments, including asymmetric half-grabens (oblique deformation), rotational shear zones, en-echelon vein arrays (bedrock faulting) and the formation of proto-transform and pure strike-slip faults. They also highlight the role of overlapping magmatic rift segments within the linkage zone, resulting in block rotation, and influencing fault architecture styles. In North Afar, Illsley-Kemp et al. (2018) and La Rosa et al. (2021) show that deformation between propagating rift segments is accommodated by oblique fault slip in a zone of diffuse strain transfer interpreted to be a proto-transform fault (Illsley-Kemp et al., 2018). Corti et al. (2019), through an integrated approach combining numerical and analog modeling, remote sensing and fieldwork investigated the Ririba Rift, Southern Ethiopia. They showed that interaction between the Ethiopian and Kenyan rift segments began with propagation of the segments, which was later aborted. The linkage zone evolved into a narrow zone of complex normal faulting with strain localization and stress-field rotation. Importantly, they demonstrate that fault propagation and abandonment processes occur over <1.5 Ma timescales, consistent with the fault age constraints we present in Figures 9 and 10. Our study thus contributes refined insights into the structural evolution of the Central Afar rift linkage zone, supporting broader, regional models of continental rift development wherein early distributed deformation transitions into focussed extension, and tectonic segments progressively evolve to accommodate strain (Acocella et al., 2008; Brune et al., 2023; Neuharth et al., 2022). While these models capture the diversity of rift linkage processes, our findings suggest a distinct structural evolution in Central Afar. We observe the initiation and development of near-symmetric, normal fault bound graben systems as the dominant method of accommodating extension due to rift linkage. This en-echelon faulting pattern, while consistent with some aspects of previous models, reflects a distinct structural style of localized deformation, differing from distributed strain and proto-transform faulting described in previous work.

6. Conclusions

In this study, we present structural constraints on the evolution timescales of seven major graben systems within the rift linkage zone between the Red Sea and Gulf of Aden rifts in Central Afar, Ethiopia. By applying quantitative geomorphology techniques to 26 catchments crossing normal faults, we resolve the timing of graben initiation to advance our understanding of rift linkage mechanisms in this zone of active continental rifting.

Using a landscape dynamics framework and stream power law analysis, we estimate the bedrock erodibility of the Afar Stratoid Basalts to range between $5.67 \times 10^{-7}\ \text{yr}^{-1} - 1.12 \times 10^{-6}\ \text{yr}^{-1}$. Knickpoint retreat metrics coupled with the relationship between footwall relief and knickpoint elevation allow us to constrain the timing of knickpoint generation, therefore the initiation of faulting. Using this data, we present a spatial model of fault segment evolution, revealing that (a) the linkage has been active in Afar for at least 3 Ma, and (b) the individual grabens accommodate rift-related extension over 0.5–1.0 Ma timescales before the strain migrates towards the rift axis along newer grabens in the center of the linkage zone.

Our analysis of fault throw rates further highlights a pronounced spatial gradient, with rates increasing towards the center of the linkage zone. We show that all the graben systems are accommodating the extension to different degrees, but the Dobi has the highest throw rates of 0.4–0.8 mm/yr, implying that Dobi is the current locus of major deformation. This finding demonstrates the dynamic nature of strain migration in rift linkage zones and aligns with the current seismicity data, showing focus of current localization and activity primarily through the center of the linkage zone. Our work also complements prior rift evolution geodynamic numerical models. This study also shows that the rift linkage in Central Afar primarily occurs through the development of en-echelon, normal fault bound graben systems, with localized extension, differing from previously proposed linkage models rift segment overlap and bookshelf faulting proposed for the area.

By integrating geomorphic metrics with structural analysis, this work provides a novel, structural based framework for quantifying fault evolution and understanding strain localization in complex continental rift systems. Our results offer critical insights into the spatio-temporal dynamics of rift propagation, with broader implications for understanding the mechanics of plate boundary zones.

Conflict of Interest

The authors declare no conflicts of interest relevant to this study.

Availability Statement

The Digital Elevation Model (DEM) used in this study is the 30-m resolution DEM from the Shuttle Radar Topography Mission (SRTM)—https://portal.opentopography.org/raster?opentopoID=OTSRTM.082015.4326.1. It is open access, available online, and can be accessed from the Tile Downloader—https://dwtkns.com/srtm30m/. Geomorphic and topographic analyses were conducted in this study using TopoToolbox, which is a MATLAB based software and code program for DEM processing and analysis. The code and function repository and the TopoToolbox programs are open source and free to download from the TopoToolbox website—https://topotoolbox.wordpress.com/ (Schwanghart & Scherler, 2014, 2017; Schwanghart et al., 2021). Maps and 3D view figures were prepared using Esri ArcGIS Pro v3.5.2. The TopoToolbox code was run in MATLAB vR2024b. The ages of the Afar Stratoid Basalt used in the calculations were taken from the open access data repository, from Tortelli et al. (2025, 2025b) Volcanism records plate thinning driven rift localization in Afar (Ethiopia) since 2–2.5 million years ago [Dataset]. In Communications Earth and Environment. Zenodo. https://doi.org/10.5281/zenodo.15197563. The earthquake data is freely available to download from the USGS NEIC seismicity catalogue—https://earthquake.usgs.gov/earthquakes/search/.

Acknowledgments

This work has received funding as project DC3 of the Marie Skłodowska-Curie Actions Doctoral Network—TALENTS, through the European Union's HORIZON-MSCA-2022-DN-01 research and innovation program under Grant 101119486 (https://www.talents-dn.eu/). RC, AW, RB, GC and DK are all beneficiaries of this Grant. DK is partially supported by the UK Research and Innovation Grant UKRI1277. We would like to thank the Associate Editor Paolo Ballato, Joe Cartwright, and two anonymous reviewers for their highly constructive comments which greatly improved the clarity and overall quality of the manuscript. Open access publishing facilitated by Universita degli Studi di Firenze, as part of the Wiley - CRUI-CARE agreement.

References

Abbate, E., Passerini, P., & Zan, L. (1995). Strike-slip faults in a rift area: A transect in the Afar triangle, East Africa. *Tectonophysics*, *241*(1–2), 67–97. https://doi.org/10.1016/0040-1951(94)00136-W

Acocella, V. (2010). Coupling volcanism and tectonics along divergent plate boundaries: Collapsed rifts from central Afar, Ethiopia. *Bulletin of the Geological Society of America*, *122*(9–10), 1717–1728. https://doi.org/10.1130/B30105.1

Acocella, V., Abebe, B., Korme, T., & Barberi, F. (2008). Structure of tendaho graben and manda harraro rift: Implications for the evolution of the Southern Red Sea propagator in central Afar. *Tectonics*, *27*(4). https://doi.org/10.1029/2007TC002236

Allen, G. H., Barnes, J. B., Pavelsky, T. M., & Kirby, E. (2013). Lithologic and tectonic controls on bedrock channel form at the northwest Himalayan front. *Journal of Geophysical Research: Earth Surface*, *118*(3), 1806–1825. https://doi.org/10.1002/jgrf.20113

Attal, M., Tucker, G. E., Whittaker, A. C., Cowie, P. A., & Roberts, G. P. (2008). Modelling fluvial incision and transient landscape evolution: Influence of dynamic channel adjustment. *Journal of Geophysical Research*, *113*(3), F03013. https://doi.org/10.1029/2007JF000893

Barberi, F., Borsi, S., Ferrara, G., Marinelli, G., Santacroce, R., Tazieff, H., & Varet, J. (1972). Evolution of the danakil depression (afar, Ethiopia) in light of radiometric age determinations. *Varet Source: The Journal of Geology*, *80*(Issue 6), 720–729. https://doi.org/10.1086/627797

Barberi, F., & Santacroce, R. (1980). The Afar stratoid series and the magmatic evolution of east African rift system. *Bulletin de la Societe Geologique de France*, *22*(6), 891–899. https://doi.org/10.2113/gssgfbull.S7-XXII.6.891

Barberi, F., & Varet, J. (1977). Volcanism of Afar: Small-scale plate tectonics implications. *GSA Bulletin*, *88*(9), 1251–1266. https://doi.org/10.1130/0016-7606(1977)88<1251:voaspt>2.0.co;2

Bastow, I. D., & Keir, D. (2011). The protracted development of the continent-ocean transition in Afar. *Nature Geoscience*, *4*(4), 248–250. https://doi.org/10.1038/ngeo1095

Bastow, I. D., Stuart, G. W., Kendall, J. M., & Ebinger, C. J. (2005). Upper-mantle seismic structure in a region of incipient Continental breakup: Northern Ethiopian rift. *Geophysical Journal International*, *162*(2), 479–493. https://doi.org/10.1111/j.1365-246X.2005.02666.x

Belachew, M., Ebinger, C., Coté, D., Keir, D., Rowland, J. v., Hammond, J. O. S., & Ayele, A. (2011). Comparison of dike intrusions in an incipient seafloor-spreading segment in Afar, Ethiopia: Seismicity perspectives. *Journal of Geophysical Research*, *116*(6), B06405. https://doi.org/10.1029/2010JB007908

Berlin, M. M., & Anderson, R. S. (2007). Modelling of knickpoint retreat on the roan Plateau, Western Colorado. *Journal of Geophysical Research*, *112*(3). https://doi.org/10.1029/2006JF000553

Beyene, A., & Abdelsalam, M. G. (2005). Tectonics of the Afar depression: A review and synthesis. *Journal of African Earth Sciences*, *41*(1–2), 41–59. https://doi.org/10.1016/j.jafrearsci.2005.03.003

Bialas, R. W., Buck, W. R., & Qin, R. (2010). How much magma is required to rift a continent? *Earth and Planetary Science Letters*, *292*(1), 68–78. https://doi.org/10.1016/j.epsl.2010.01.021

Bonini, M., Corti, G., Innocenti, F., Manetti, P., Mazzarini, F., Abebe, T., & Pecskay, Z. (2005). Evolution of the main Ethiopian rift in the frame of Afar and Kenya rifts propagation. *Tectonics*, *24*(1), 1–21. https://doi.org/10.1029/2004TC001680

Bonnefille, R., Potts, R., Chalié, F., Jolly, D., & Peyron, O. (2004). High-resolution vegetation and climate change associated with Pliocene Australopithecus afarensis. Retrieved from https://www.pnas.org

Boulton, S. J., Stokes, M., & Mather, A. E. (2014). Transient fluvial incision as an indicator of active faulting and plio-quaternary uplift of the Moroccan high atlas. *Tectonophysics*, *633*(1), 16–33. https://doi.org/10.1016/j.tecto.2014.06.032

Boulton, S. J., & Whittaker, A. C. (2009). Quantifying the slip rates, spatial distribution, and evolution of active normal faults from geomorphic analysis: Field examples from an oblique-extensional graben, southern Turkey. *Geomorphology*, *104*(3–4), 299–316. https://doi.org/10.1016/j.geomorph.2008.09.007

Brune, S., Kolawole, F., Olive, J.-A., Stamps, D. S., Buck, W. R., Buiter, S. J. H., et al. (2023). Geodynamics of Continental rift initiation and evolution. *Nature Reviews Earth and Environment*, *4*(4), 235–253. https://doi.org/10.1038/s43017-023-00391-3

Chauvet, F., Geoffroy, L., le Gall, B., & Jaud, M. (2023). Volcanic passive margins and break-up processes in the Southern Red Sea. *Gondwana Research*, *117*, 169–193. https://doi.org/10.1016/j.gr.2023.01.004

Cherkose, B. A., Issa, S., Saibi, H., & ElHaj, K. (2023). Building a geospatial model to identify potential geothermal sites in ayrobera: Afar depression, NE Ethiopia. *Geothermics*, *110*, 102689. https://doi.org/10.1016/j.geothermics.2023.102689

Chernet, T., Hart, W. K., Aronson, J. L., & Walter, R. C. (1998). New age constraints on the timing of volcanism and tectonism in the northern main Ethiopian Rift–southern Afar transition zone (ethiopia). *Journal of Volcanology and Geothermal Research*, *80*(3), 267–280. https://doi.org/10.1016/S0377-0273(97)00035-8

Commins, D., Gupta, S., & Cartwright, J. (2005). Deformed streams reveal growth and linkage of a normal fault array in the canyonlands graben, Utah. *Geology*, *33*(8), 645–648. https://doi.org/10.1130/G21433AR.1

Corti, G. (2009). Continental rift evolution: From rift initiation to incipient break-up in the main Ethiopian rift, East Africa. *Earth-Science Reviews*, *96*(Issues 1–2), 1–53. https://doi.org/10.1016/j.earscirev.2009.06.005

Corti, G., Bastow, I. D., Keir, D., Pagli, C., & Baker, E. (2015). Rift-related morphology of the Afar depression. In P. Billi (Ed.), *Landscapes and landforms of Ethiopia* (pp. 251–274). Springer. https://doi.org/10.1007/978-94-017-8026-1_15

Corti, G., Cioni, R., Franceschini, Z., Sani, F., Scaillet, S., Molin, P., et al. (2019). Aborted propagation of the Ethiopian rift caused by linkage with the Kenyan rift. *Nature Communications*, *10*(1), 1309. https://doi.org/10.1038/s41467-019-09335-2

Courtillot, V., Achache, J., Landre, F., Bonhommet, N., Montigny, R., & Féraud, G. (1984). Episodic spreading and rift propagation: New paleomagnetic and geochronologic data from the Afar nascent passive margin. *Journal of Geophysical Research*, *89*(B5), 3315–3333. https://doi.org/10.1029/JB089iB05p03315

Dambly, M. L. T., Samrock, F., Grayver, A. v., & Saar, M. O. (2023). Insights on the interplay of rifting, transcrustal magmatism and formation of geothermal resources in the central segment of the Ethiopian rift revealed by 3-D magnetotelluric imaging. *Journal of Geophysical Research: Solid Earth*, *128*(7), e2022JB025849. https://doi.org/10.1029/2022JB025849

Dan, W., Wang, Q., Tang, G. J., & Zhang, X. Z. (2025). Magmatism in Continental rifts and rifted margins. In *Science China Earth sciences*. Science China Press. https://doi.org/10.1007/s11430-024-1623-5

D'Arcy, M., & Whittaker, A. C. (2014). Geomorphic constraints on landscape sensitivity to climate in tectonically active areas. *Geomorphology*, *204*, 366–381. https://doi.org/10.1016/j.geomorph.2013.08.019

Densmore, A. L., Dawers, N. H., Gupta, S., Allen, P. A., & Gilpin, R. (2003). Landscape evolution at extensional relay zones. *Journal of Geophysical Research*, *108*(B5), 2273. https://doi.org/10.1029/2001jb001741

DiMaggio, E. N., Arrowsmith, J. R., Campisano, C. J., Johnson, R., Deino, A. L., Warren, M., et al. (2015). Tephrostratigraphy and depositional environment of young (<2.94 Ma) hadar formation deposits at ledi-geraru, Afar, Ethiopia. *Journal of African Earth Sciences*, *112*, 234–250. https://doi.org/10.1016/j.jafrearsci.2015.09.018

Doubre, C., Déprez, A., Masson, F., Socquet, A., Lewi, E., Grandin, R., et al. (2017). Current deformation in central Afar and triple junction kinematics deduced from GPS and InSAR measurements. *Geophysical Journal International*, *208*(2), 936–953. https://doi.org/10.1093/gji/ggw434

Doubre, C., Manighetti, I., Dorbath, C., Dorbath, L., Jacques, E., & Delmond, J. C. (2007). Crustal structure and magmato-tectonic processes in an active rift (Asal-Ghoubbet, Afar, East Africa): 1. Insights from a 5-month seismological experiment. *Journal of Geophysical Research*, *112*(5). https://doi.org/10.1029/2005JB003940

Duclaux, G., Huismans, R. S., & May, D. A. (2020). Rotation, narrowing, and preferential reactivation of brittle structures during oblique rifting. *Earth and Planetary Science Letters*, *531*, 115952. https://doi.org/10.1016/j.epsl.2019.115952

Duvall, A., Kirby, E., & Burbank, D. (2004). Tectonic and lithologic controls on bedrock channel profiles and processes in coastal California. *Journal of Geophysical Research*, *109*(F3). https://doi.org/10.1029/2003jf000086

Ebinger, C. J., & Casey, M. (2001). Continental breakup in magmatic provinces: An Ethiopian example. *Geology*, *29*(6), 527–530. https://doi.org/10.1130/0091-7613(2001)029<0527:CBIMPA>2.0.CO;2

Farr, T. G., Rosen, P. A., Caro, E., Crippen, R., Duren, R., Hensley, S., et al. (2007). The shuttle radar topography mission. *Reviews of Geophysics*, *45*(2). https://doi.org/10.1029/2005RG000183

Feyissa, D. H., Kitagawa, H., Bizuneh, T. D., Tanaka, R., Kabeto, K., & Nakamura, E. (2019). Transition from plume-driven to plate-driven magmatism in the evolution of the main Ethiopian rift. *Journal of Petrology*, *60*(8), 1681–1715. https://doi.org/10.1093/petrology/egz043

Gailleton, B., Mudd, S. M., Clubb, F. J., Grieve, S. W. D., & Hurst, M. D. (2021). Impact of changing concavity indices on channel steepness and divide migration metrics. *Journal of Geophysical Research: Earth Surface*, *126*(10), e2020JF006060. https://doi.org/10.1029/2020JF006060

Gailleton, B., Sinclair, H. D., Mudd, S. M., Graf, E. L. S., & Maţenco, L. C. (2021). Isolating lithologic versus tectonic signals of river profiles to test orogenic models for the eastern and southeastern carpathians. *Journal of Geophysical Research: Earth Surface*, *126*(8), e2020JF005970. https://doi.org/10.1029/2020JF005970

Gallen, S. F., & Fernández-Blanco, D. (2021). A new data-driven bayesian inversion of fluvial topography clarifies the tectonic history of the corinth rift and reveals a channel steepness threshold. *Journal of Geophysical Research: Earth Surface*, *126*(3), e2020JF005651. https://doi.org/10.1029/2020JF005651

Gallen, S. F., & Wegmann, K. W. (2017). River profile response to normal fault growth and linkage: An example from the Hellenic forearc of south-central Crete, Greece. *Earth Surface Dynamics*, *5*(1), 161–186. https://doi.org/10.5194/esurf-5-161-2017

Gasparini, N. M., & Brandon, M. T. (2011). A generalized power law approximation for fluvial incision of bedrock channels. *Journal of Geophysical Research*, *116*(F2). https://doi.org/10.1029/2009JF001655

Gasparini, N. M., Fischer, G. C., Adams, J. M., Dawers, N. H., & Janoff, A. M. (2016). Morphological signatures of normal faulting in low-gradient alluvial Rivers in south-eastern Louisiana, USA. *Earth Surface Processes and Landforms*, *41*(5), 642–657. https://doi.org/10.1002/esp.3852

Gasparini, N. M., & Whipple, K. X. (2014). Diagnosing climatic and tectonic controls on topography: Eastern flank of the northern Bolivian andes. *Lithosphere*, *6*(4), 230–250. https://doi.org/10.1130/L322.1

Gasse, E., & Street, F. A. (1978). Late Quaternary Lake-level fluctuations and environments of the northern rift valley and Afar region (ethiopia and Djibouti). *Palaeogeography, Palaeoclimatology, Palaeoecology*, *24*(4), 279–325. https://doi.org/10.1016/0031-0182(78)90011-1

Gasse, F., Richard, O., Robbe, D., Rognon, P., & Williams, M. (1980). Evolution tectonique et climatique de l'Afar central d'apres les sediments plio-pleistocenes. *Bulletin de la Societe Geologique de France*, *S7-XXII*(6), 987–1001. https://doi.org/10.2113/gssgfbull.S7-XXII.6.987

Geiger, F. L. (2014). Landscape evolution of the needles fault zone, Utah, investigated through chronostratigraphic and terrain analyses. *All Graduate Theses and Dissertations, Spring 1920 to Summer*, *3885*, 2023.

Hack, J. T. (1957). Studies of longitudinal stream profiles in Virginia and Maryland. In *Professional paper*. https://doi.org/10.3133/pp294B

Harel, M. A., Mudd, S. M., & Attal, M. (2016). Global analysis of the stream power law parameters based on worldwide 10Be denudation rates. In *Geomorphology*, Vol. 268, 184–196. Elsevier B.V. https://doi.org/10.1016/j.geomorph.2016.05.035

Harkins, N., Kirby, E., Heimsath, A., Robinson, R., & Reiser, U. (2007). Transient fluvial incision in the headwaters of the yellow river, northeastern Tibet, China. *Journal of Geophysical Research*, *112*(3), F03S04. https://doi.org/10.1029/2006JF000570

Hayward, N. J., & Ebinger, C. J. (1996). Variations in the along-axis segmentation of the Afar rift system. *Tectonics*, *15*(2), 244–257. https://doi.org/10.1029/95TC02292

Hurman, G. L., Keir, D., Bull, J. M., McNeill, L. C., Booth, A. D., & Bastow, I. D. (2023). Quantitative analysis of faulting in the Danakil depression rift of Afar: The importance of faulting in the final stages of magma-rich rifting. *Tectonics*, *42*(6), e2022TC007607. https://doi.org/10.1029/2022TC007607

Illsley-Kemp, F., Bull, J. M., Keir, D., Gerya, T., Pagli, C., Gernon, T., et al. (2018). Initiation of a proto-transform fault prior to seafloor spreading. *Geochemistry, Geophysics, Geosystems*, *19*(12), 4744–4756. https://doi.org/10.1029/2018GC007947

Jolie, E., Scott, S., Faulds, J., Chambefort, I., Axelsson, G., Gutiérrez-Negrín, L. C., et al. (2021). Geological controls on geothermal resources for power generation. In *Nature Reviews Earth and Environment*, Vol. 2(5), 324–339. Springer Nature. https://doi.org/10.1038/s43017-021-00154-y

Keir, D., Bastow, I. D., Pagli, C., & Chambers, E. L. (2013). The development of extension and magmatism in the Red Sea rift of Afar. *Tectonophysics*, *607*, 98–114. https://doi.org/10.1016/j.tecto.2012.10.015

Keir, D., Hamling, I. J., Ayele, A., Calais, E., Ebinger, C., Wright, T. J., et al. (2009). Evidence for focused magmatic accretion at segment centers from lateral dike injections captured beneath the Red Sea rift in Afar. *Geology*, *37*(1), 59–62. https://doi.org/10.1130/G25147A.1

Kendall, J. M., Stuart, G. W., Ebinger, C. J., Bastow, I. D., & Keir, D. (2005). Magma-assisted rifting in Ethiopia. *Nature*, *433*(7022), 146–148. https://doi.org/10.1038/nature03161

Kent, E., Boulton, S. J., Whittaker, A. C., Stewart, I. S., & Cihat Alçiçek, M. (2017). Normal fault growth and linkage in the gediz (alaşehir) Graben, Western Turkey, revealed by transient river long-profiles and slope-break knickpoints. *Earth Surface Processes and Landforms*, *42*(5), 836–852. https://doi.org/10.1002/esp.4049

Kent, E., Whittaker, A. C., Boulton, S. J., & Alçiçek, M. C. (2021). Quantifying the competing influences of lithology and throw rate on bedrock River incision. *Bulletin of the Geological Society of America*, *133*(7–8), 1649–1664. https://doi.org/10.1130/B35783.1

Kidane, T., Courtillot, V., Manighetti, I., Audin, L., Lahitte, P., Quidelleur, X., et al. (2003). New paleomagnetic and geochronologic results from Ethiopian Afar: Block rotations linked to rift overlap and propagation and determination of a ∼2 Ma reference pole for stable Africa. *Journal of Geophysical Research*, *108*(B2). https://doi.org/10.1029/2001jb000645

Kirby, E., & Whipple, K. (2001). Quantifying differential rock-uplift rates via stream profile analysis. *Geology*, *29*(5), 415–418. https://doi.org/10.1130/0091-7613(2001)029<0415:QDRURV>2.0.CO;2

Kirby, E., & Whipple, K. X. (2012). Expression of active tectonics in erosional landscapes. *Journal of Structural Geology*, *44*, 54–75. https://doi.org/10.1016/j.jsg.2012.07.009

Kobor, J. S., & Roering, J. J. (2004). Systematic variation of bedrock channel gradients in the central Oregon Coast range: Implications for rock uplift and shallow landsliding. *Geomorphology*, *62*(3–4), 239–256. https://doi.org/10.1016/j.geomorph.2004.02.013

Lahitte, P., Gillot, P.-Y., Kidane, T., Courtillot, V., & Bekele, A. (2003). New age constraints on the timing of volcanism in central Afar, in the presence of propagating rifts. *Journal of Geophysical Research*, *108*(B2). https://doi.org/10.1029/2001JB001689

La Rosa, A., Gayrin, P., Brune, S., Pagli, C., Muluneh, A. A., Tortelli, G., & Keir, D. (2025). Cross-scale strain analysis in the Afar rift (east Africa) from automatic fault mapping and geodesy. *Solid Earth*, *16*(10), 929–945. https://doi.org/10.5194/se-16-929-2025

La Rosa, A., Pagli, C., Hurman, G. L., & Keir, D. (2022). Strain accommodation by intrusion and faulting in a rift linkage zone: Evidences from high-resolution topography data of the afrera plain (afar, East Africa). *Tectonics*, *41*(6), e2021TC007115. https://doi.org/10.1029/2021TC007115

La Rosa, A., Pagli, C., Wang, H., Doubre, C., Leroy, S., Sani, F., et al. (2021). Plate-boundary kinematics of the afrera linkage zone (afar) from InSAR and seismicity. *Journal of Geophysical Research: Solid Earth*, *126*(5), e2020JB021387. https://doi.org/10.1029/2020JB021387

Ledésert, B. A., Hébert, R. L., Mouchot, J., Bosia, C., Ravier, G., Seibel, O., et al. (2021). Scaling in a geothermal heat exchanger at soultz-sous-forêts (upper rhine graben, France): A XRD and SEM-EDS characterization of sulfide precipitates. *Geosciences*, *11*(7), 271. https://doi.org/10.3390/geosciences11070271

Leonard, J. S., Whipple, K. X., & Heimsath, A. M. (2023). Isolating climatic, tectonic, and lithologic controls on Mountain landscape evolution. https://doi.org/10.1126/sciadv.add8915

Leroy, S., Lucazeau, F., D'Acremont, E., Watremez, L., Autin, J., Rouzo, S., et al. (2010). Contrasted styles of rifting in the eastern gulf of Aden: A combined wide-angle, multichannel seismic, and heat flow survey. In *Geochemistry, Geophysics, Geosystems*, Vol. 11(7). Blackwell Publishing Ltd. https://doi.org/10.1029/2009GC002963

Levin, N. E., Quade, J., Simpson, S. W., Semaw, S., & Rogers, M. (2004). Isotopic evidence for Plio–Pleistocene environmental change at gona, Ethiopia. *Earth and Planetary Science Letters*, *219*(1), 93–110. https://doi.org/10.1016/S0012-821X(03)00707-6

Maestrelli, D., Sani, F., Keir, D., Pagli, C., Rosa, A. l., Muluneh, A. A., et al. (2024). Reconciling plate motion and faulting at a rift-rift-rift triple junction. *Geology*, *52*(5), 362–366. https://doi.org/10.1130/G51909.1

Manighetti, I., Tapponnier, P., Courtillot, V., Gallet, Y., Jacques, E., & Gillot, P. Y. (2001). Strain transfer between disconnected, propagating rifts in Afar. *Journal of Geophysical Research*, *106*(B7), 13613–13665. https://doi.org/10.1029/2000jb900454

Manighetti, I., Tapponnier, P., Gillot, P. Y., Jacques, E., Courtillot, V., Armijo, R., et al. (1998). Propagation of rifting along the arabia-somalia plate boundary: Into Afar. *Journal of Geophysical Research*, *103*(3), 4947–4974. https://doi.org/10.1029/97jb02758

McClusky, S., Reilinger, R., Ogubazghi, G., Amleson, A., Healeb, B., Vernant, P., et al. (2010). Kinematics of the southern red sea-afar triple junction and implications for plate dynamics. *Geophysical Research Letters*, *37*(5). https://doi.org/10.1029/2009GL041127

Merle, O. (2011). A simple Continental rift classification. *Tectonophysics*, *513*(1–4), 88–95. https://doi.org/10.1016/j.tecto.2011.10.004

Miller, S. R., Baldwin, S. L., & Fitzgerald, P. G. (2012). Transient fluvial incision and active surface uplift in the woodlark rift of eastern Papua New Guinea. *Lithosphere*, *4*(2), 131–149. https://doi.org/10.1130/L135.1

Mitchell, N. A., & Yanites, B. J. (2019). Spatially variable increase in rock uplift in the northern U.S. Cordillera recorded in the distribution of river knickpoints and incision depths. *Journal of Geophysical Research: Earth Surface*, *124*(5), 1238–1260. https://doi.org/10.1029/2018JF004880

Moore, C., Wright, T. J., & Hooper, A. (2021). Rift focusing and magmatism during late-stage rifting in Afar. *Journal of Geophysical Research: Solid Earth*, *126*(10), e2020JB021542. https://doi.org/10.1029/2020JB021542

Muirhead, J. D., Kattenhorn, S. A., Lee, H., Mana, S., Turrin, B. D., Fischer, T. P., et al. (2016). Evolution of upper crustal faulting assisted by magmatic volatile release during early-stage continental rift development in the East African rift. *Geosphere*, *12*(6), 1670–1700. https://doi.org/10.1130/GES01375.1

Muluneh, A., Brune, S., Pagli, C., la Rosa, A., Keir, D., Neuharth, D., & Corti, G. (2024). To rotate or to link? The connection between the Red Sea and gulf of Aden rifts in central Afar. *Geophysical Research Letters*, *51*(12), e2024GL108732. https://doi.org/10.1029/2024GL108732

Muluneh, A. A., Kidane, T., Rowland, J., & Bachtadse, V. (2013). Counterclockwise block rotation linked to southward propagation and overlap of sub-aerial Red Sea rift segments, Afar depression: Insight from paleomagnetism. *Tectonophysics*, *593*, 111–120. https://doi.org/10.1016/j.tecto.2013.02.030

NASA Shuttle Radar Topography Mission (SRTM). (2013). Shuttle radar topography mission (SRTM) global [Dataset]. *Distributed by OpenTopography*. https://doi.org/10.5069/G9445JDF

Nelson, W. R., Furman, T., van Keken, P. E., Shirey, S. B., & Hanan, B. B. (2012). OsHf isotopic insight into mantle plume dynamics beneath the east African rift system. *Chemical Geology*, *320–321*, 66–79. https://doi.org/10.1016/j.chemgeo.2012.05.020

Neuharth, D., Brune, S., Wrona, T., Glerum, A., Braun, J., & Yuan, X. (2022). Evolution of rift systems and their fault networks in response to surface processes. *Tectonics*, *41*(3), e2021TC007166. https://doi.org/10.1029/2021TC007166

Nixon, C. W., McNeill, L. C., Bull, J. M., Bell, R. E., Gawthorpe, R. L., Henstock, T. J., et al. (2016). Rapid spatiotemporal variations in rift structure during development of the corinth rift, Central Greece. *Tectonics*, *35*(5), 1225–1248. https://doi.org/10.1002/2015TC004026

Nixon, C. W., McNeill, L. C., Gawthorpe, R. L., Shillington, D. J., Michas, G., Bell, R. E., et al. (2024). Increasing fault slip rates within the corinth rift, Greece: A rapidly localising active rift fault network. *Earth and Planetary Science Letters*, *636*, 118716. https://doi.org/10.1016/j.epsl.2024.118716

Oliva, S. J., Ebinger, C. J., Wauthier, C., Muirhead, J. D., Roecker, S. W., Rivalta, E., & Heimann, S. (2019). Insights into fault-magma interactions in an early-stage Continental rift from source mechanisms and correlated volcano-tectonic earthquakes. *Geophysical Research Letters*, *46*(4), 2065–2074. https://doi.org/10.1029/2018GL080866

Pagli, C., Wang, H., Wright, T. J., Calais, E., & Lewi, E. (2014). Current plate boundary deformation of the Afar rift from a 3-D velocity field inversion of InSAR and GPS. *Journal of Geophysical Research: Solid Earth*, *119*(11), 8562–8575. https://doi.org/10.1002/2014JB011391

Pagli, C., Yun, S. H., Ebinger, C., Keir, D., & Wang, H. (2019). Strike-slip tectonics during rift linkage. *Geology*, *47*(1), 31–34. https://doi.org/10.1130/G45345.1

Pan, S., Bell, R. E., Jackson, C. A. L., & Naliboff, J. (2022). Evolution of normal fault displacement and length as Continental lithosphere stretches. *Basin Research*, *34*(1), 121–140. https://doi.org/10.1111/bre.12613

Pavano, F., Pazzaglia, F. J., & Catalano, S. (2016). Knickpoints as geomorphic markers of active tectonics: A case study from northeastern sicily (southern Italy). *Lithosphere*, *8*(6), 633–648. https://doi.org/10.1130/L577.1

Pechlivanidou, S., Cowie, P. A., Duclaux, G., Nixon, C. W., Gawthorpe, R. L., & Salles, T. (2019). Tipping the balance: Shifts in sediment production in an active rift setting. *Geology*, *47*(3), 259–262. https://doi.org/10.1130/G45589.1

Polun, S. G., Horrell, D., Tesfaye, S., & Gomez, F. (2024). Readjustment of fluvial systems to Quaternary tectonic disruption in the central Afar (ethiopia). *Geomorphology*, *455*, 109192. https://doi.org/10.1016/j.geomorph.2024.109192

Pritchard, D., Roberts, G. G., White, N. J., & Richardson, C. N. (2009). Uplift histories from river profiles. *Geophysical Research Letters*, *36*(24). https://doi.org/10.1029/2009GL040928

Quye-Sawyer, J., Whittaker, A. C., Roberts, G. G., & Rood, D. H. (2021). Fault throw and regional uplift histories from drainage analysis: Evolution of southern Italy. *Tectonics*, *40*(4), e2020TC006076. https://doi.org/10.1029/2020TC006076

Rime, V., Foubert, A., Atnafu, B., & Kidane, T. (2022). Geological map of the Southern Red Sea and Western gulf of Aden region. https://doi.org/10.5281/zenodo.7351643

Rime, V., Foubert, A., Ruch, J., & Kidane, T. (2023). Tectonostratigraphic evolution and significance of the Afar depression. In *Earth-Science Reviews*, Vol. 244, 104519. Elsevier B.V. https://doi.org/10.1016/j.earscirev.2023.104519

Rime, V., Keir, D., Phethean, J., Kidane, T., & Foubert, A. (2024). Central Afar: An analogue for Oceanic Plateau development. *Geology*, *52*(11), 819–824. https://doi.org/10.1130/G52330.1

Roberts, G. G., White, N. J., Martin-Brandis, G. L., & Crosby, A. G. (2012). An uplift history of the colorado Plateau and its surroundings from inverse modelling of longitudinal river profiles. *Tectonics*, *31*(4). https://doi.org/10.1029/2012TC003107

Roda-Boluda, D. C., & Whittaker, A. C. (2017). Structural and geomorphological constraints on active normal faulting and landscape evolution in Calabria, Italy. https://doi.org/10.6084/m9.figshare.c.3689464

Roda-Boluda, D. C., & Whittaker, A. C. (2018). Normal fault evolution and coupled landscape response: Examples from the southern apennines, Italy. *Basin Research*, *30*(S1), 186–209. https://doi.org/10.1111/bre.12215

Rowland, J. v., Baker, E., Ebinger, C. J., Keir, D., Kidane, T., Biggs, J., et al. (2007). Fault growth at a nascent slow-spreading ridge: 2005 dabbahu rifting episode, Afar. *Geophysical Journal International*, *171*(3), 1226–1246. https://doi.org/10.1111/j.1365-246X.2007.03584.x

Royden, L., & Taylor Perron, J. (2013). Solutions of the stream power equation and application to the evolution of river longitudinal profiles. *Journal of Geophysical Research: Earth Surface*, *118*(2), 497–518. https://doi.org/10.1002/jgrf.20031

Saria, E., Calais, E., Stamps, D. S., Delvaux, D., & Hartnady, C. J. H. (2014). Present-day kinematics of the east African rift. *Journal of Geophysical Research: Solid Earth*, *119*(4), 3584–3600. https://doi.org/10.1002/2013JB010901

Schwanghart, W., Molkenthin, C., & Scherler, D. (2021). A systematic approach and software for the analysis of point patterns on river networks [SOFTWARE]. *Earth Surface Processes and Landforms*, *46*(9), 1847–1862. https://doi.org/10.1002/esp.5127

Schwanghart, W., & Scherler, D. (2014). Short communication: topoToolbox 2 - MATLAB-Based software for topographic analysis and modelling in Earth surface sciences [SOFTWARE]. *Earth Surface Dynamics*, *2*(1), 1–7. https://doi.org/10.5194/esurf-2-1-2014

Schwanghart, W., & Scherler, D. (2017). Bumps in river profiles: Uncertainty assessment and smoothing using quantile regression techniques [SOFTWARE]. *Earth Surface Dynamics*, *5*(4), 821–839. https://doi.org/10.5194/esurf-5-821-2017

Sembroni, A., Molin, P., Pazzaglia, F. J., Faccenna, C., & Abebe, B. (2016). Evolution of continental-scale drainage in response to mantle dynamics and surface processes: An example from the Ethiopian Highlands. *Geomorphology*, *261*, 12–29. https://doi.org/10.1016/j.geomorph.2016.02.022

Siegburg, M., Bull, J. M., Nixon, C. W., Keir, D., Gernon, T. M., Corti, G., et al. (2020). Quantitative constraints on faulting and fault slip rates in the northern main Ethiopian rift. *Tectonics*, *39*(8), e2019TC006046. https://doi.org/10.1029/2019TC006046

Smail, I. E., Rector, A. L., Robinson, J. R., & Reed, K. E. (2025). Pliocene climatic change and the origins of homo at ledi-Geraru, Ethiopia. *Annals of Human Biology*, *52*(1), 2462255. https://doi.org/10.1080/03014460.2025.2462255

Smith, A. G. G., & Fox, M. (2024). When does the concavity index constrain stream power parameters? *Journal of Geophysical Research: Earth Surface*, *129*(9), e2023JF007584. https://doi.org/10.1029/2023JF007584

Snyder, N. P., Whipple, K. X., Tucker, G. E., & Merritts, D. J. (2000). Landscape response to tectonic forcing: Digital elevation model analysis of stream profiles in the mendocino triple junction region, northern California. *GSA Bulletin*, *112*(8), 1250–1263. https://doi.org/10.1130/0016-7606(2000)112<1250:LRTTFD>2.0.CO;2

Snyder, N. P., Whipple, K. X., Tucker, G. E., & Merritts, D. J. (2003). Channel response to tectonic forcing: Field analysis of stream morphology and hydrology in the mendocino triple junction region, northern California. *Geomorphology*, *53*(1–2), 97–127. https://doi.org/10.1016/S0169-555X(02)00349-5

Stock, J. D., & Montgomery, D. R. (1999). Geologic constraints on bedrock river incision using the stream power law. *Journal of Geophysical Research*, *104*(B3), 4983–4993. https://doi.org/10.1029/98jb02139

Stucky de Quay, G., Roberts, G. G., Rood, D. H., & Fernandes, V. M. (2019). Holocene uplift and rapid fluvial erosion of Iceland: A record of post-glacial landscape evolution. *Earth and Planetary Science Letters*, *505*, 118–130. https://doi.org/10.1016/j.epsl.2018.10.026

Stüwe, K., Robl, J., Turab, S. A., Sternai, P., & Stuart, F. M. (2022). Feedbacks between sea-floor spreading, trade winds and precipitation in the Southern Red Sea. *Nature Communications*, *13*(1), 5405. https://doi.org/10.1038/s41467-022-32293-1

Tapponnier, P., Armijo, R., Manighetti, I., & Courtillot, V. (1990). Bookshelf faulting and horizontal block rotations between overlapping rifts in southern Afar. *Geophysical Research Letters*, *17*(1), 1–4. https://doi.org/10.1029/GL017i001p00001

Teklay, M., Scherer, E. E., Mezger, K., & Danyushevsky, L. (2010). Geochemical characteristics and sr-nd-hf isotope compositions of mantle xenoliths and host basalts from assab, Eritrea: Implications for the composition and thermal structure of the lithosphere beneath the Afar depression. *Contributions to Mineralogy and Petrology*, *159*(5), 731–751. https://doi.org/10.1007/s00410-009-0451-0

Tierney, J. E., deMenocal, P. B., & Zander, P. D. (2017). A climatic context for the out-of-africa migration. *Geology*, *45*(11), 1023–1026. https://doi.org/10.1130/G39457.1

Tortelli, G., Gioncada, A., Pagli, C., Barfod, D. N., Corti, G., Sani, F., et al. (2025a). Volcanism records plate thinning driven rift localization in Afar (ethiopia) since 2-2.5 million years ago. *Communications Earth & Environment*, *6*(1), 395. https://doi.org/10.1038/s43247-025-02356-4

Tortelli, G., Gioncada, A., Pagli, C., Barfod, D. N., Corti, G., Sani, F., et al. (2025b). Volcanism records plate thinning driven rift localization in Afar (ethiopia) since 2-2.5 million years ago [Dataset]. *Zenodo*. In *Communications Earth and environment*. https://doi.org/10.5281/zenodo.15197563

Tortelli, G., Gioncada, A., Pagli, C., Braschi, E., Gebru, E. F., & Keir, D. (2022). Constraints on the magma source and rift evolution from geochemistry of the stratoid flood basalts (afar, Ethiopia). *Geochemistry, Geophysics, Geosystems*, *23*(8), e2022GC010434. https://doi.org/10.1029/2022GC010434

Tortelli, G., Gioncada, A., Pagli, C., Braschi, E., Gebru, E. F., & Keir, D. (2024). From melt-to crystal-rich magmatic systems during rift localization: Insights from mineral chemistry in central Afar (ethiopia). *Contributions to Mineralogy and Petrology*, *179*(10), 87. https://doi.org/10.1007/s00410-024-02164-7

Trauth, M. H., Maslin, M. A., Deino, A., & Strecker, M. R. (2005). Late Cenozoic moisture history of East Africa. *Science*, *309*(5743), 2051–2053. https://doi.org/10.1126/science.1112964

Trudgill, B. D. (2002). Structural controls on drainage development in the canyonlands grabens of southeast Utah. *AAPG Bulletin*, *86*(6), 1095–1112. https://doi.org/10.1306/61EEDC2E-173E-11D7-8645000102C1865D

Tucker, G. E., & Whipple, K. X. (2002). Topographic outcomes predicted by stream erosion models: Sensitivity analysis and intermodel comparison. *Journal of Geophysical Research*, *107*(B9). https://doi.org/10.1029/2001jb000162

United States Geological Survey (USGS). (2025). Earthquakes, "Search Earthquake Catalogue" [Dataset]. Retrieved from https://earthquake.usgs.gov/earthquakes/search/

Watts, E. J., Rees, R., Jonathan, P., Keir, D., Taylor, R. N., Siegburg, M., et al. (2025). Mantle upwelling at Afar triple junction shaped by overriding plate dynamics. *Nature Geoscience*, *18*(7), 661–669. https://doi.org/10.1038/s41561-025-01717-0

Wedmore, L. N. J., Evans, D., Williams, J. N., Biggs, J., Fagereng, Å., Mawejje, P., et al. (2024). The early onset of magmatic rift faulting in the edward-george rift, Uganda. *Earth and Planetary Science Letters*, *638*, 118762. https://doi.org/10.1016/j.epsl.2024.118762

Wedmore, L. N. J., Turner, T., Biggs, J., Williams, J. N., Sichingabula, H. M., Kabumbu, C., & Banda, K. (2022). The luangwa rift active fault database and fault reactivation along the Southwestern branch of the east African rift. *Solid Earth*, *13*(11), 1731–1753. https://doi.org/10.5194/se-13-1731-2022

Whipple, K. X., & Tucker, G. E. (1999). Dynamics of the stream-power river incision model: Implications for height limits of Mountain ranges, landscape response timescales, and research needs. *Journal of Geophysical Research*, *104*(B8), 17661–17674. https://doi.org/10.1029/1999jb900120

Whipple, K. X., & Tucker, G. E. (2002). Implications of sediment-flux-dependent river incision models for landscape evolution. *Journal of Geophysical Research*, *107*(2). https://doi.org/10.1029/2000jb000044

White, S. M., Crisp, J. A., & Spera, F. J. (2006). Long-term volumetric eruption rates and magma budgets. *Geochemistry, Geophysics, Geosystems*, *7*(3). https://doi.org/10.1029/2005GC001002

Whittaker, A. C. (2012). How do landscapes record tectonics and climate? *Lithosphere*, *4*(2), 160–164. https://doi.org/10.1130/RF.L003.1

Whittaker, A. C., & Boulton, S. J. (2012). Tectonic and climatic controls on knickpoint retreat rates and landscape response times. *Journal of Geophysical Research*, *117*(2). https://doi.org/10.1029/2011JF002157

Whittaker, A. C., Cowie, P. A., Attal, M., Tucker, G. E., & Roberts, G. P. (2007a). Bedrock channel adjustment to tectonic forcing: Implications for predicting river incision rates. *Geology*, *35*(2), 103–106. https://doi.org/10.1130/G23106A.1

Whittaker, A. C., Cowie, P. A., Attal, M., Tucker, G. E., & Roberts, G. P. (2007b). Contrasting transient and steady-state Rivers crossing active normal faults: New field observations from the central apennines, Italy. *Basin Research*, *19*(4), 529–556. https://doi.org/10.1111/j.1365-2117.2007.00337.x

Whittaker, A. C., & Walker, A. S. (2015). Geomorphic constraints on fault throw rates and linkage times: Examples from the northern gulf of evia, Greece. *Journal of Geophysical Research: Earth Surface*, *120*(1), 137–158. https://doi.org/10.1002/2014JF003318

Williams, J. N., Wedmore, L. N. J., Scholz, C. A., Kolawole, F., Wright, L. J. M., Shillington, D. J., et al. (2022). The Malawi active fault database: An onshore-offshore database for regional assessment of seismic hazard and tectonic evolution. *Geochemistry, Geophysics, Geosystems*, *23*(5), e2022GC010425. https://doi.org/10.1029/2022GC010425

Wolfenden, E., Ebinger, C., Yirgu, G., Renne, P. R., & Kelley, S. P. (2005). Evolution of a volcanic rifted margin: Southern Red Sea, Ethiopia. *GSA Bulletin*, *117*(7–8), 846–864. https://doi.org/10.1130/B25516.1

Zhou, Z., Whittaker, A. C., Bell, R. E., & Hampson, G. J. (2024). Unravelling tectonic and lithological effects on transient landscapes in the Gulf of Corinth, Greece. *Basin Research*, *36*(5), e12901. https://doi.org/10.1111/bre.12901

Zondervan, J. R., Whittaker, A. C., Bell, R. E., Watkins, S. E., Brooke, S. A. S., & Hann, M. G. (2020). New constraints on bedrock erodibility and landscape response times upstream of an active fault. *Geomorphology*, *351*, 106937. https://doi.org/10.1016/j.geomorph.2019.106937

Zwaan, F., Alves, T. M., Cadenas, P., Gouiza, M., Phethean, J. J. J., Brune, S., & Glerum, A. C. (2024). (D)rifting in the 21st century: Key processes, natural hazards, and geo-resources. In *Solid Earth*, Vol. 15(8), 989–1028. Copernicus Publications. https://doi.org/10.5194/se-15-989-2024

Zwaan, F., Corti, G., Keir, D., & Sani, F. (2020). A review of tectonic models for the rifted margin of Afar: Implications for Continental break-up and passive margin formation. In *Journal of African Earth Sciences*, Vol. 164, 103649. Elsevier Ltd. https://doi.org/10.1016/j.jafrearsci.2019.103649